Experimental study of homogeneous nucleation from the bismuth supersaturated vapor: Evaluation of the surface tension of critical nucleus

A. A. Onischuk, S. V. Vosel, O. V. Borovkova, A. M. Baklanov, V. V. Karasev et al.

Citation: J. Chem. Phys. **136**, 224506 (2012); doi: 10.1063/1.4725535
View online: http://dx.doi.org/10.1063/1.4725535
View Table of Contents: http://jcp.aip.org/resource/1/JCPSA6/v136/i22
Published by the American Institute of Physics.

Experimental study of homogeneous nucleation from the bismuth supersaturated vapor: Evaluation of the surface tension of critical nucleus

A. A. Onischuk,[1,2] S. V. Vosel,[1,2] O. V. Borovkova,[1] A. M. Baklanov,[1] V. V. Karasev,[1] and S. di Stasio[3]
[1]*Institute of Chemical Kinetics and Combustion, Novosibirsk 630090, Russia*
[2]*Novosibirsk State University, Novosibirsk 630090, Russia*
[3]*Istituto Motori CNR-IM Aerosol and Nanostructures Lab., Via Marconi 8, Napoli 80125, Italy*

(Received 12 March 2012; accepted 16 May 2012; published online 13 June 2012)

The homogeneous nucleation of bismuth supersaturated vapor is studied in a laminar flow quartz tube nucleation chamber. The concentration, size, and morphology of outcoming aerosol particles are analyzed by a transmission electron microscope (TEM) and an automatic diffusion battery (ADB). The wall deposit morphology is studied by scanning electron microscopy. The rate of wall deposition is measured by the light absorption technique and direct weighting of the wall deposits. The confines of the nucleation region are determined in the "supersaturation cut-off" measurements inserting a metal grid into the nucleation zone and monitoring the outlet aerosol concentration response. Using the above experimental techniques, the nucleation rate, supersaturation, and nucleation temperature are measured. The surface tension of the critical nucleus and the radius of the surface of tension are determined from the measured nucleation parameters. To this aim an analytical formula for the nucleation rate is used, derived from author's previous papers based on the Gibbs formula for the work of formation of critical nucleus and the translation-rotation correction. A more accurate approach is also applied to determine the surface tension of critical drop from the experimentally measured bismuth mass flow, temperature profiles, ADB, and TEM data solving an inverse problem by numerical simulation. The simulation of the vapor to particles conversion is carried out in the framework of the explicit finite difference scheme accounting the nucleation, vapor to particles and vapor to wall deposition, and particle to wall deposition, coagulation. The nucleation rate is determined from simulations to be in the range of 10^9–10^{11} cm^{-3} s^{-1} for the supersaturation of Bi_2 dimers being 10^{17}–10^7 and the nucleation temperature 330–570 K, respectively. The surface tension σ_S of the bismuth critical nucleus is found to be in the range of 455–487 mN/m for the radius of the surface of tension from 0.36 to 0.48 nm. The function σ_S changes weakly with the radius of critical nucleus. The value of σ_S is from 14% to 24% higher than the surface tension of a flat surface. © *2012 American Institute of Physics*. [http://dx.doi.org/10.1063/1.4725535]

I. INTRODUCTION

The surface curvature dependence of surface tension is a central problem in the surface termodynamics.[1] A detailed understanding of the curvature dependence of interfacial properties is important in many applications, such as homogeneous nucleation, adhesion, enhanced solubility of small particles, retention, and flow of liquids in porous materials. It is hardly possible to measure directly the curvature dependence of surface tension. However, there are many theoretical contributions in the literature where the surface tension σ_S of a small drop was calculated as a function of its radius R. A considerable fraction of theoretical papers used the density functional theories to determine the function $\sigma_S(R)$.[2–12] In these papers the surface tension was found to be a non-monotonic function of drop radius. In some papers thermodynamic treatments were applied[13] using additional empirical observations. The molecular dynamics[14–17] as well as Monte Carlo simulation[18] was also used to study the dependence of surface tension on the drop radius. However, most often the numerical simulation can be applied for a rather narrow class of model systems such as Lennard-Jones (L-J) fluids for which the interaction potential is known. In the case of real systems such as water, organics, and others the modeling is much more complicated and further efforts are necessary to work out new methodologies which can allow determining the surface tension as function of radius. One of the ways in this direction is to evaluate the small drop surface tension from the homogeneous nucleation rate I_{nucl} measured experimentally for certain temperature and supersaturation.[19] However, this approach is viable only if a rigorous formula which put into relationship the surface tension σ_S and the nucleation rate I_{nucl} is available.

The classical nucleation theory (CNT) is in a strong disagreement with the experimentally measured nucleation rates (see, for example, Ref. 20). The reason for this disagreement is that CNT uses the surface tension (σ_∞) for a flat surface which gives most often an error of tens orders of magnitude in estimating the nucleation rate. Another problem with the classical formula for the nucleation rate is in the fact that it does not consider the contribution to the free energy from the translation and rotation of the critical drop. The problem of the translation-rotation correction factor was discussed in the literature during the last five decades. Frenkel[21] was the

first who argued that the three translational and three rotational degrees of freedom of the critical drop must be accounted properly in the formula for the nucleation rate. Lothe and Pound[22,23] have proposed a way to calculate this contribution in the framework of Gibbs process of drop formation. Reiss *et al.*[24,25] have offered an approach to account the translational degrees of freedom. Kusaka[26] has used the Lothe-Pound theory as a basis and derived a rigorous formula for the correction factor. One should note that the theory of Lothe-Pound and Kusaka for correction factor accounts the dependence of surface tension on radius automatically. However, the formula of Kusaka can be used only in numerical calculations for simple systems such as L-J ones. In a previous work we proposed an analytical formula for the correction factor[27] which is to multiply the classical expression for the nucleation rate to account the translation and rotation of the critical nucleus. The formula is based on the Kusaka's theory, the theory of Reiss accounting the translational degrees of freedom of the center of mass of the drop, and Frenkel's kinetic theory of liquids. This formula is in a good agreement with the Kusaka simulation results for the L-J system and can be applied to any real system of interest. Besides, the formula for Zeldovitch factor is to be derived accounting the dependence of surface tension on the drop radius. This derivation was done in Refs. 19, 20, and 28. Thus, now we have a rigorous formula accounting both the $\sigma_S(R)$ dependence and translation-rotation correction factor which allows us to calculate the dependence of the surface tension on radius from the experimental nucleation rate.

Most of the studies of the homogeneous nucleation have been devoted to molecular liquids. Metals are a very different class of substances. Delocalized electrons are the reason for their typical metallic properties including high surface tension. However, the quantitative information on the nucleation rate from the supersaturated metal vapor is quite scarce. There are experimental measurements of the nucleation rate for monovalent Li,[29] Na,[30] Cs,[31–33] Ag,[19,34] and bivalent metals Mg,[35] Zn,[19] Hg.[36,37] The nucleation rate was also calculated from first principles for Li, Na, K, Rb, Ag, Au,[38] Zn,[39] Al,[40] and Fe.[41] In this work we present a systematic study on the homogeneous nucleation from the bismuth supersaturated vapor.

It was discussed in Refs. 19 and 20 that the surface tension of critical nuclei for the elements of the I group of the Periodic Table is higher than that of the flat surface and comes down with the increasing radius. For the elements of the II group the surface tension of critical nuclei is less than that of the flat surface and does not changes essentially with radius. Bismuth is the element of the V group, for which any predictions are not yet available to scientific community.

The objective of this paper is to study the homogeneous nucleation of bismuth supersaturated vapor in a laminar flow nucleation chamber. We will delimit the region of the nucleation chamber where the nucleation is significant and determine the nucleation rate, temperature, and supersaturation ratio in this region. A rough estimation of the surface tension and radius of the critical nucleus from the experimental nucleation parameters will be done. Afterwards we will perform a numerical simulation to get the magnitude of the surface tension of critical nucleus and the radius of the surface of tension more accurately. This simulation is to clarify how much is the difference between surface tension of critical nuclei and that of a flat surface and if the ratio σ_S/σ_∞ is larger or less than unity. Also the functionality of $\sigma_S(R)$ dependence will be analyzed to quantify how strong can be the variations of surface tension with the drop radius.

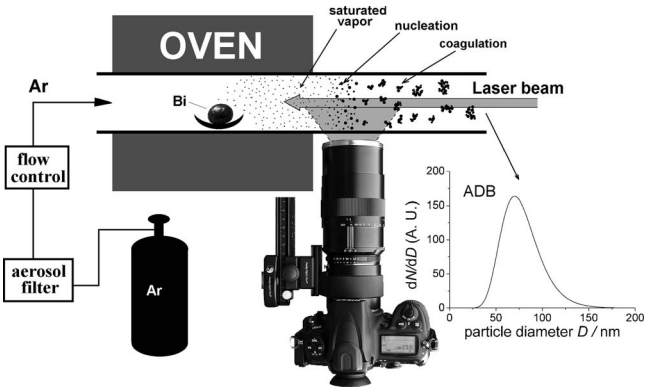

FIG. 1. Scheme of the experimental setup. Frequency distribution function for bismuth aerosol diameter (ADB measurement) is shown as an example for the heating temperature (i.e., the temperature in the isothermal zone of the oven) $T_H = 1080$ K and measurement axial coordinate $z = 32$ cm ($z = 0$ corresponds to the outlet edge of the oven).

II. EXPERIMENTAL

The experiments on bismuth vapor nucleation are carried out in a horizontal laminar flow nucleation chamber (Fig. 1). The nucleation chamber consists of a horizontal quartz tube with the inner diameter of 0.68 cm, and an outer three sectional oven. A flux of Ar is supplied to the inlet of the tube. Before entering the nucleation chamber the gas passes through a high efficiency Petrianov aerosol filter.[42] The inlet Ar flow rate is $Q_0 = 8.3$ cm^3/s (at room temperature and atmospheric pressure). About the middle of the heated section an isothermal high temperature zone is formed. Before the experiment a crucible with pellets of bismuth was charged into the isothermal zone as a feedstock. The axial and radial temperature profiles are measured by a *K*-type thermocouple (upflow directed) with a bare junction diameter of 100 μm. In the isothermal zone the undersaturated vapor is formed. As the bismuth vapor flow along the mainstream of the Ar gas flow it becomes saturated and thereafter supersaturated owing to the temperature decrease along the tube. Finally, the homogeneous nucleation rate became high enough to make the particle formation substantial. Most often in our experiments the nucleation occurred at temperature less than the melting point, i.e., the nucleation resulted in the formation of solid particles, which grew due to the vapor deposition. The vapor to particle deposition is accompanied by the coagulation of particles, which results in the formation of aggregates consisting of small primary particles.

The size and shape of aggregates are studied by transmission electron microscopes (TEM) EM 910 LEO and JEM 100SX. The sampling for TEM is carried out by a thermophoretical precipitator.[43] The particles are deposited on an electron microscopy grid covered with polyvinyl formal or carbon film. Besides, the aerosol size spectrum and

particle number concentration are measured by an automatic diffusion battery (ADB) coupled with a condensation nucleus counter.[44] This device is able to measure the particle size distribution in the range of 3–200 nm and the aerosol concentration in the range of $10^1-5\times10^5$ cm^{-3} directly and up to 10^9 cm^{-3} using the aerosol dilution technique.[45] To measure the particle concentration in the range of 10^5–10^9 a three cascade diluter is used. The first cascade unit is to decrease the aerosol concentration by mixing the aerosol with the pure Ar or air. To this aim an ejecting system or just three way mixing junction is used. The other two cascades section splits the aerosol flux into two ones, filtering one of these and mixing the fluxes again. The first cascade unit gives the dilution ratio from 10 to 100 and the other section results in the diluting coefficient of 100.

The morphology of wall deposit is studied by a scanning electron microscope (SEM) LEO-1430. For this purpose a thin quartz filament of diameter 1 mm is fixed longitudinally upon the inner surface of the flow chamber (at the bottom) before the start of the nucleation experiment. The run is performed at constant flow and temperature during the time of 30–200 min. After stop experiment the filament is removed from the chamber, cut to pieces, and the deposit of bismuth on it is observed by SEM.

The light scattering is used for monitoring larger than 0.1 μm particles in the nucleation chamber. A semiconductor laser KLM-650/20 (wavelength of 650 nm, power in the beam of 20 mW) is used. The laser beam is directed in parallel to the axis. The 90° light scattering image is recorded by a digital camera "EOS 50" with a micro objective (see Fig. 1). The light scattering onset coordinate is determined by analyzing the axial profiles of scattering intensity.

The "supersaturation cut-off" method[46] is used to find approximate dimensions of the nucleation zone. The idea of this method is in inserting a stainless steel grid inside the nucleation region. The vapor to grid deposition results in the suppression of nucleation downflow, which is observed as a decrease of outlet aerosol concentration. The outlet concentration vs. axial grid position curve has a dip, which gives approximate confines of the nucleation zone. In more detail this method will be described in Sec. III.

III. RESULTS

Some examples of the axial and wall temperatures as functions of axial coordinate are shown in Fig. 2. When measuring the wall temperature profile the thermocouple junction was touching the wall making the angle of 45° with the axis. A typical example of the radial temperature profile is shown in Fig. 3. The vertical diametric temperature profile is slightly asymmetrical and well approximated by the parabolic function being shifted upwards by 0.02 mm with respect to the axis. The temperature of the isothermal zone of the oven (which we refer to as the heating temperature T_H) was in the range 750–1150 K. Typical size distribution for bismuth aerosol is shown in the inset of Fig. 1 as measured by ADB at the outlet of the flow chamber at the axial coordinate $z = 32$ cm (the position $z = 0$ corresponds to the outlet edge of the oven). To demonstrate the range of aerosol concentrations Fig. 4(a) shows the aerosol number concentration as measured

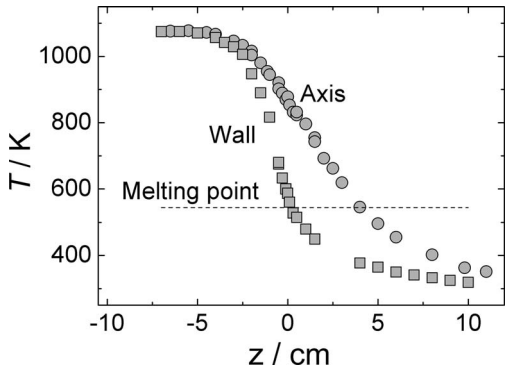

FIG. 2. Wall and axial temperature profiles. Heating temperature is $T_H = 1080$ K.

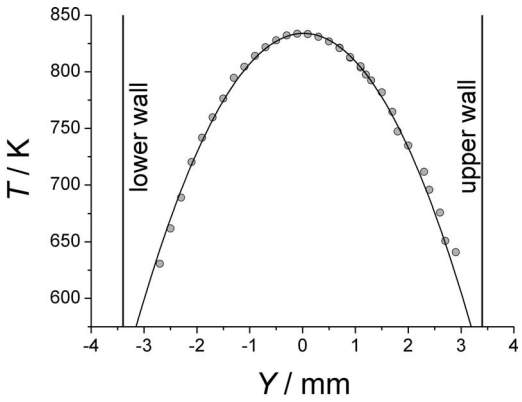

FIG. 3. An example of vertical diametric temperature profile. Heating temperature is $T_H = 1080$ K, axial coordinate $z = 0.5$ cm. Solid line is the parabolic function $T(Y) = 834–25.8(Y(\text{mm}) - 0.02)^2$. Y is vertical coordinate ($Y = 0$ corresponds to the axis of tube).

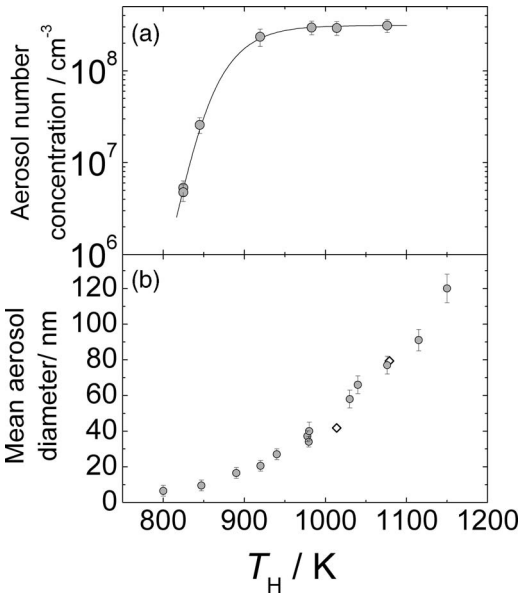

FIG. 4. (a) Aerosol number concentration and (b) mean arithmetic aerosol diameter at the outlet of nucleation chamber vs. heating temperature. Circles: ADB measurement results; diamonds: TEM elaboration results; and line: eye guide.

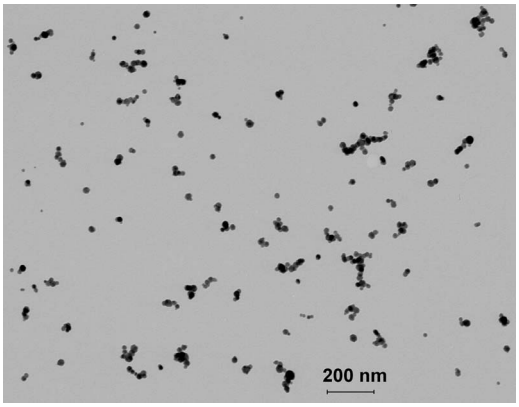

FIG. 5. TEM image of Bi nanoparticles sampled at the outlet of nucleation chamber, $z = 32$ cm. Heating temperature $T_H = 1080$ K.

by the ADB at the outlet of nucleation chamber as a function of heating temperature T_H. A typical TEM image of bismuth particles as sampled at the outlet of the nucleation chamber is shown in Fig. 5. One can see that aerosol is formed as aggregates consisting of small primary particles. The mean number of primary particles per aggregate was determined from TEM images to be $\gamma_{prim} = 11 \pm 2$ and 4 ± 1 for $T_H = 1080$ and 1014 K, respectively. The aggregate morphology can be described in terms of the so-called fractal-like dimension D_f. The estimation of the fractal-like dimensionality will be used later in this work to link the aggregate mass and size in numerical simulations (see Sec. IV C). Therefore, in the following we are giving some details of the experimental measurements of D_f. The aggregate geometric radius R_a is determined from the elaboration of TEM images. For each aggregate in the image it is calculated as

$$R_a = \frac{1}{2}\sqrt{LW}, \tag{1}$$

where L and W are the length and width of the smallest rectangle enclosing the single aggregate image. The fractal-like dimension can be determined from a power relationship between the aggregate mass M and radius R_a measured in the TEM analysis[45,47–50]

$$M = kR_a^{D_f}, \tag{2}$$

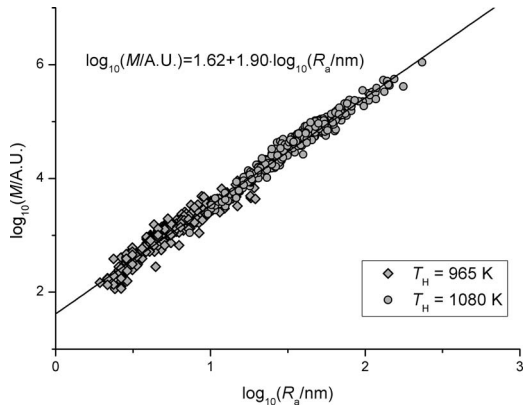

FIG. 6. Aggregate mass vs. aggregate radius in logarithmic coordinates as determined from TEM images elaboration. $T_H = 965$ (diamonds) and 1080 K (circles). Solid line corresponds to the fractal-like dimension $D_f = 1.90$.

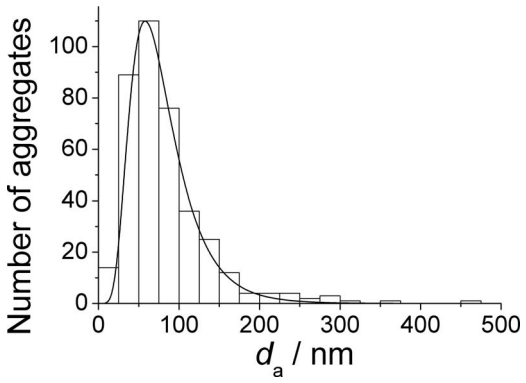

FIG. 7. Frequency distribution over aggregate geometric diameters (TEM images elaboration). Heating temperature $T_H = 1080$ K. Sampling coordinate $z = 32$ cm. Solid line follows the log-normal law with the standard geometric deviation $\sigma_g = 1.6$.

where k is a constant. To find the aggregate mass (in arbitrary units) we determined the total greyness of each individual aggregate in the TEM image. The image is elaborated as a file in format "bmp." The total greyness is determined as the sum of the gray values of all the pixels, which constitute the aggregate image. A correction to the background greyness is also done. It is assumed that the local greyness in the aggregate image is proportional to the local thickness of the original aggregate. Therefore, the mass of the original aggregate is considered to be proportional to the total greyness of the aggregate image. This approach seems to be reasonable because it is known that the fractal-like dimension of two-dimensional projection is approximately equal to the D_f of the original 3D object if $D_f < 2$.[47,48] Figure 6 shows the aggregate mass vs. aggregate radius plot in logarithmic coordinates as determined from TEM images elaboration. The aggregates from different heating temperatures are characterized by the same fractal-like dimension $D_f = 1.90 \pm 0.01$.

The mean diameter of outlet aggregates vs. heating temperature is shown in Fig. 4(b) as determined from both the ADB measurements and the TEM elaboration for identical experimental conditions. A good agreement between the ADB data and TEM elaborations can be seen which is not surprising because it is known that the equivalent mobility radius is close to both the mean projection and the geometric ones.[49,51] Figures 7 and 8 give examples of the frequency distributions

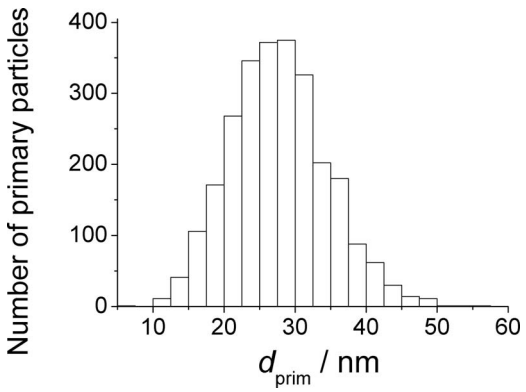

FIG. 8. Frequency distribution over primary particles diameters (TEM images elaboration). Heating temperature $T_H = 1080$ K. Sampling coordinate $z = 32$ cm.

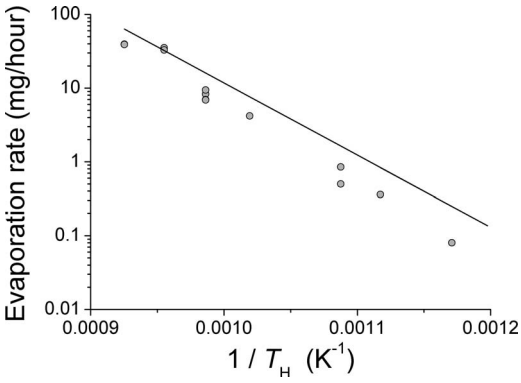

FIG. 9. The rate of bismuth evaporation from the crucible in the isothermal zone vs. heating temperature (symbols); line corresponds to the saturated vapor (see Table I).

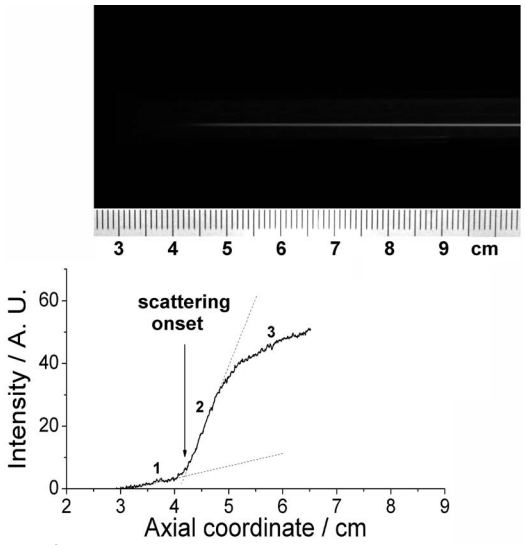

FIG. 10. Upper frame: an example of light scattering image. The axial coordinate z is shown (zero is the outlet edge of oven); lower plot: scattering intensity axial profile for the upper frame. Heating temperature T_H = 1080 K. The laser beam passes in the axial-vertical plane (in parallel to the axis) 0.3 cm from the lower wall.

over the aggregate and primary particle diameters. The aggregate size distribution function follows the log-normal law with the standard geometric deviation $\sigma_g = 1.6$ (this magnitude of σ_g will be used in the numerical simulations of Sec. IV C). Figure 9 shows the rate of bismuth evaporation from the crucible in the isothermal zone as a function of heating temperature. This rate is determined by weighting the crucible with bismuth before and after the run at constant heating temperature. The saturation line is calculated from the saturated vapor partial pressures of Bi and Bi_2 molecules (see Table I). As can be seen from the plot the bismuth vapor in the evaporation zone is from 40% to 70% undersaturated.

To evaluate the nucleation rate as well as the temperature and supersaturation corresponding to this rate it is important to know the location and dimensions of the nucleation zone. Thereto different techniques can be useful. Some experimental methods can be applied in a wide range of heating temperature (such as ADB, for example). Other facilities can be used only for high enough heating temperatures when the mass concentration of bismuth in the gas phase is substantial (aerosol filter deposition for mass analysis, wall deposit mass measurements by weighting, light scattering from aerosol, and others). The "supersaturation cut-off" technique is good for low heating temperatures and cannot be used for high temperatures $T_H > 1100$ K because of the grid being blocked by the vapor deposition. Therefore, it is selected a temperature ($T_H = 1080$ K) for which all the techniques can be used and a cross comparison of the experimental measurements is done.

Figure 10 shows a typical light scattering image (upper picture) and the light scattering axial profile for this frame (lower picture). Three regions can be seen in scattering profile: (1) background light, (2) scattering growth due to the increase of the nucleation rate (and particle diameters) with z, and (3) the saturation region. The crossing of dash lines from regions 1 and 2 gives the scattering onset coordinate, which should be near to the maximum nucleation rate zone. Figure 11 shows the axial-vertical scattering onset coordinate plot. In these measurements the beam passes in the axial-vertical plane. One can see that the symmetry axis of the plot is shifted a bit upwards with respect to the tube axis, which is probably caused by a small contribution from the thermal convection. One can conclude from the plot that as the gas moves along the tube the nucleation starts first near the walls and then spreads to the axis.

Figure 12 shows the wall deposit images after 1.1 h of deposition at $T_H = 1080$ K. One can distinguish a few typical zones. At $z < -3.3$ cm the clean walls not covered by deposit are observed. Then in the region $-3.3 < z < -2.1$ the deposit is formed and single islands are well discernible (we refer to this kind of deposit as island-like). At $z \approx -2.1$ cm one can

TABLE I. Physical-chemical parameters for bismuth.

Saturation vapor total pressure over the molten liquid bismuth,[52–55] (Pa)	$P^0 = 3.41 \times 10^{10}\exp(-22860/T)$ (544.5 < T < 1200 K)
Partial pressure of Bi molecules in the saturated bismuth vapor,[53,54,56] (Pa)	$P^0_{Bi} = 1.83 \times 10^{10}\exp(-23310/T)$ (500 < T < 1100 K)
Partial pressure of Bi_2 molecules in the saturated bismuth vapor,[54–56] (Pa)	$P^0_{Bi2} = 1.87 \times 10^{10}\exp(-22670/T)$ (500 < T < 1100 K)
Surface tension for flat interface,[52] mN/m	$\sigma_\infty = 425.5 - 8.0 \times 10^{-2} \times T$
Molten bismuth density,[52] (kg/m^3)	$\rho = 10730 - 1.221 \times T$
Sound velocity in molten bismuth,[52] (m/s)	$u = 2.111 \times 10^3 - 0.797 \times T$
Melting point,[52] (K)	$T_m = 544.4$

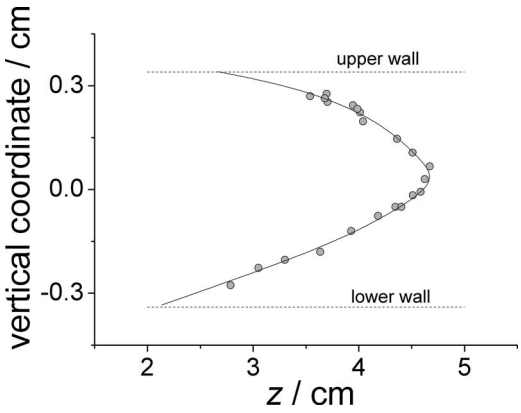

FIG. 11. Light scattering onset coordinate plot. Vertical coordinate passes through the axis of the tube. Heating temperature $T_H = 1080$ K. Solid line is an eye guide.

see a transition from the island-like deposit to a thick layer. At $z > 3$ cm the deposit is powder-like which is due to the fact that the vapor wall deposition rate becomes small with respect to the rate of particle to wall deposition. The SEM images illustrate the different kind morphologies of the deposit.

Figure 13 shows the deposit profile measured by the light absorption for different deposition times, i.e., for different values of deposited bismuth total mass. A Xe-gas white cold cathode fluorescent lamp is used as a light source in the light absorption experiments. The clean walls to islands and islands to thick layer transitions can be seen as step-like changes of the absorption intensity. The coordinate for the islands to thick layer transition is a function of the deposition time. The absolute mass profile is determined in separate experiments. In these experiments the reactor was run at constant temperature and flow rate during a period of time of 1–3 h. Then, after the experiment the tube was cut to pieces and weighted, then the deposit was removed by nitric acid in water solution and the pieces were rinsed with pure water and weighted again. Figure 14 gives an example of the wall deposit axial profile as determined by weighting the pieces of the tube. The

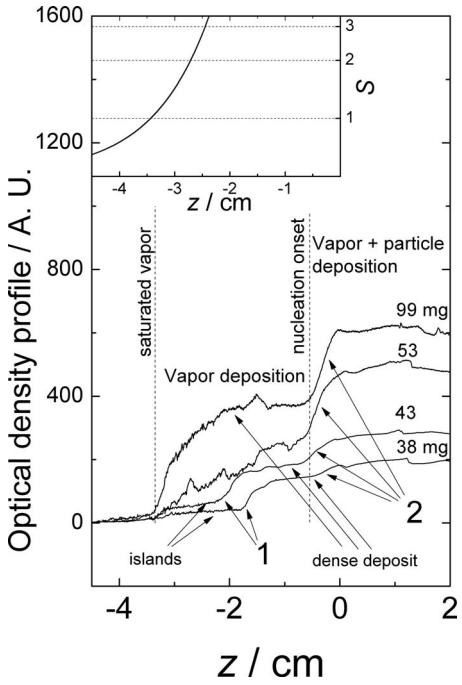

FIG. 13. Light absorption axial profiles of wall deposit for different deposition times. Mass deposit total weight is shown for each curve. Heating temperature $T_H = 1080$ K. The supersaturation near the wall surface as a function of z is shown in the inset (calculated from the experimental wall temperature profile (Fig. 2), evaporation rate in the isothermal zone (Fig. 9), and partial pressures P^0_{Bi} and P^0_{Bi2} (Table I)). The run time from bottom to top is 1.0; 1.1; 1.5; 3.0 h.

solid and dashed lines represent the results of two experiment trials.

To evaluate the approximate length of the nucleation volume the "supersaturation cut-off" experiments are carried out. The procedure used in the experiment is shown in the drawings of Fig. 15. A stainless steel wire circular grid (with 13.8 mesh per cm and the wire diameter 0.2 mm) with diameter equal to the inner tube size is inserted to the nucleation chamber perpendicularly to the flow to overlap the tube cross section. The outlet aerosol concentration is monitored by the

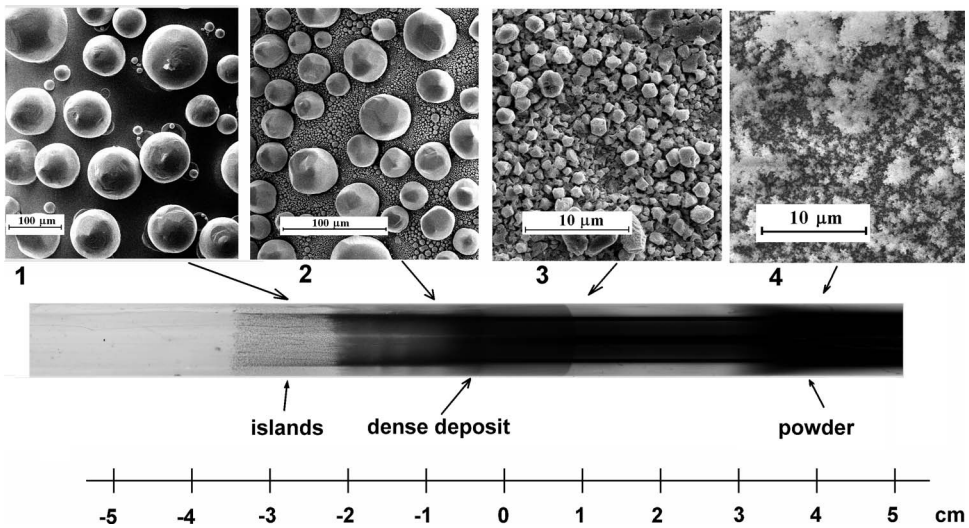

FIG. 12. SEM images of deposit for different axial coordinates (upper images) and transparence microscopic image of the nucleation chamber tube (lower image) after 1.1 h of running at heating temperature $T_H = 1080$ K. Total mass of deposit is 43 mg. Axial coordinate z is shown; zero corresponds to the outlet edge of the heater.

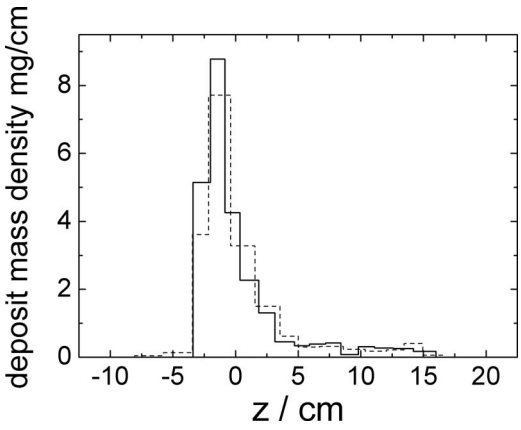

FIG. 14. Deposit density (mass per unit length of the tube) vs. the axial coordinate. Heating temperature $T_H = 1080$ K. The results of two trials are shown. The time of deposition is 1.1 h.

ADB as the grid is moving upflow. Initially, i.e., when the grid is downflow far from the nucleation zone (see the upper drawing), the outlet concentration is not disturbed by the presence of grid owing to the fact that the particle to grid deposition is negligible due to the low particle diffusion coefficient. When the grid is inserted to the nucleation zone (middle drawing), the vapor to grid deposition results in the suppression of homogeneous nucleation downflow after the grid but the particles formed before come freely through the grid. Thus, when moving the grid upflow through the nucleation zone we decrease the volume of nucleation. When the grid is just at the nucleation onset position the outlet aerosol concentration is the lowest as the total nucleation volume has been cut off by the grid (lower drawing). When moving the grid even more upflow to the supersaturation less than unity zone the vapor to grid deposition rate is zero which results in the increase of the outlet particle concentration to the value of without grid measurements. Examples of the outlet aerosol concentration vs. grid axial position dependence are shown in Fig. 16 for different heating temperatures. It is important to know the scale of the temperature disturbance induced by the grid insertion to the nucleation chamber. Figure 17 shows the temperature axial profiles with and without the grid inserted to the nucleation chamber. One can see that the temperature disturbance zone is about 0.4 cm, which is comparable with axial accuracy in the "supersaturation cut-off" experiments.

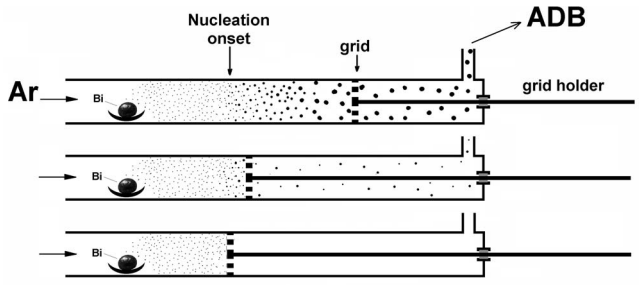

FIG. 15. Scheme of the "supersaturation cut-off" experiment.

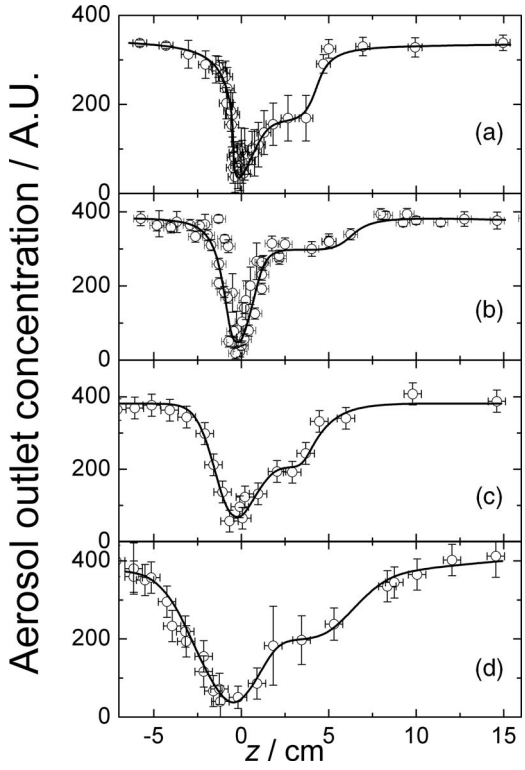

FIG. 16. "Supersaturation cut-off" experiments results: outlet aerosol concentration vs. axial position of grid. The heating temperatures $T_H = 1080$ (a), 1014 (b), 920 (c), and 854 K (d). The solid lines are eye guides.

IV. DISCUSSION

In this section we will consider in more detail the experimental data for the heating temperature $T_H = 1080$ K to give a comparison for different techniques. First, we will consider the effect of vapor association. Afterwards, we will discuss the mechanism of vapor to particle conversion and the details of numerical simulation for this process. Finally, we will compare the simulation results with the experimental data and discuss the surface tension of critical nuclei for different radii and nucleation temperatures as determined from the simulations.

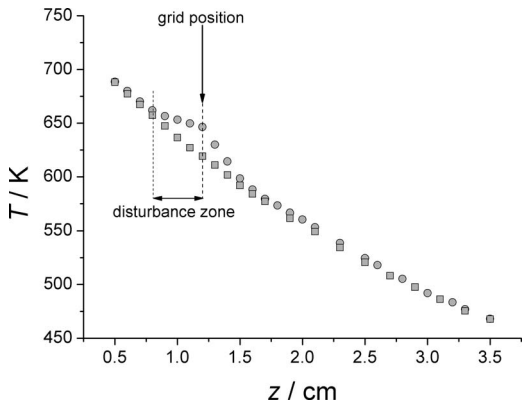

FIG. 17. Axial temperature profiles in the nucleation chamber with the grid inserted (circles) and without grid (squares). The thermocouple junction position was shifted 0.6 mm vertically (downwards) and 1.1 mm horizontally from the axis. Heating temperature $T_H = 1014$ K.

A. Effect of vapor association: Kelvin equation for associated vapor

The vapor of bismuth exhibits appreciable association being a mixture of Bi and Bi_2 molecules. The ratio between the partial pressures $P^0_{Bi_2}$ and P^0_{Bi} of these species in the saturated vapor can be approximated by (see Table I and Refs. 53–56)

$$\frac{P^0_{Bi_2}}{P^0_{Bi}} = 1.02 \exp\left(\frac{640}{T}\right), \tag{3}$$

where T is temperature. Thus, for example, for $T = 700$ and 500 K we get $\frac{P^0_{Bi_2}}{P^0_{Bi}} = 2.5$ and 3.7, respectively. As the association equilibrium occurs in the supersaturated vapor as well we have

$$K = \frac{\left(P^0_{Bi}\right)^2}{P^0_{Bi_2}} = \frac{(P_{Bi})^2}{P_{Bi_2}}, \tag{4}$$

where K is the equilibrium constant, P_{Bi} and P_{Bi_2} are the partial pressures for the Bi and Bi_2 species in the supersaturated vapor, respectively. Then, from Eq. (4) we have

$$\frac{\alpha_0^2}{1-\alpha_0} = \frac{S\alpha^2}{1-\alpha}, \tag{5}$$

where α and α_0 are molar fractions of Bi atoms in supersaturated and saturated vapor, respectively, and S is the supersaturation ratio ($\alpha = \frac{P_{Bi}}{P_{Bi}+P_{Bi_2}}$, $\alpha_0 = \frac{P^0_{Bi}}{P^0_{Bi}+P^0_{Bi_2}}$, $S = \frac{P}{P^0} = \frac{P_{Bi}+P_{Bi_2}}{P^0_{Bi}+P^0_{Bi_2}}$, P^0 is the saturated vapor pressure). For small α, Eq. (5) can be rewritten as

$$\alpha \approx \frac{\alpha_0}{\sqrt{1-\alpha_0}} \frac{1}{\sqrt{S}}. \tag{6}$$

It will be shown in Sec. IV C that in our case the typical supersaturation ratio S in the nucleation volume is in the range of 10^7–10^{17} at nucleation temperature 600–330 K. Hence, as follows from Eqs. (3) and (6) the fraction of monomers in supersaturated vapor is equal to 10^{-4}–10^{-9}. Therefore, in the following calculations of the mass transfer in the supersaturated vapor we consider the vapor as composed by Bi_2 molecules only. However, the supersaturation S in the nucleation zone may differ by about 20% from the supersaturation of dimmers $S_2 = \frac{P_{Bi_2}}{P^0_{Bi_2}}$, which is to be accounted in the thermodynamic equations. In particular, the association effect is to be accounted in the formula connecting the radius of the critical nucleus with the supersaturation ratio. In Ref. 57 this connection was obtained in the framework of CNT. In the next part of this section we give a more rigorous derivation of the relationship between the critical radius and supersaturation using the Gibbs theory of interface.[1]

Let us consider a liquid drop being in equilibrium with a macroscopic partly associated vapor phase consisting of both monomers Bi and dimmers Bi_2. In accordance with the theory of Gibbs we introduce a spherical dividing surface between the drop and the outer phase, called surface of tension, of radius R_S. The volumes outside and inside the dividing surface are filled, respectively, by the macroscopic homogeneous phases α and β (the so-called reference phases). The phases α and β have the same nature as the real outer phase and the drop, respectively. The temperature and chemical potentials for Bi and Bi_2 in the phases α and β are equal to these in the real system. Thus, for monomers we have

$$\mu_1^\beta(P^\beta, T) = \mu_1 = \mu_1^\alpha\left(P_1^\alpha, T\right), \tag{7}$$

where $\mu_1^\alpha(P_1^\alpha, T)$, $\mu_1^\beta(P^\beta, T)$, and μ_1 are the chemical potentials for monomers in the macroscopic reference phases α and β, and the real system, respectively; P^β is total pressure in the phase β, and P_1^α is the partial pressure of monomers in the phase α. One should note that P_1^α is equal to the partial pressure of monomers P_{Bi} in the gas-phase of real system far from interface. In the case of flat dividing surface Eq. (7) transforms to

$$\mu_1^\beta(P^0, T) = \mu_1^\alpha\left(P_1^{0,\alpha}, T\right), \tag{8}$$

where P^0 and $P_1^{0,\alpha}$ are the pressure in the phase β and partial pressure of monomers in the phase α, respectively, in the case of flat surface (one should note that in the phase α the total pressure is P^0 as well).

In the approximation of ideal gas and incompressible liquid Eq. (7) can be rewritten in the following form:

$$\mu_1^\beta(P^0, T) + \left(\frac{\partial \mu_1^\beta}{\partial P}\right)_{P^0,T} (P^\beta - P^0) = \mu_1^\alpha\left(P_1^{0,\alpha}, T\right) + kT \ln\left(\frac{P_1^\alpha}{P_1^{0,\alpha}}\right), \tag{9}$$

where the LHS is the expansion in a Taylor series about P^0 (the second and higher order terms are equal to zero due to the incompressibility approximation). For small enough drops when $P^\beta \gg P^0$ we can change $P^\beta - P^0$ for $P^\beta - P^\alpha$, where P^α is the total vapor pressure in the phase α. Then taking into account that $V_{Bi} = (\frac{\partial \mu_1^\beta}{\partial P})_{P^0,T}$ (V_{Bi} is the volume per monomer in the phase β), $S_1 = \frac{P_1^\alpha}{P_1^{0,\alpha}}$, and subtracting Eq. (8) from Eq. (9) we obtain

$$V_{Bi}(P^\beta - P^\alpha) = kT \ln S_1. \tag{10}$$

Taking into account the Laplace equation[1]

$$P^\beta - P^\alpha = \frac{2\sigma(R_S)}{R_S}, \tag{11}$$

where $\sigma(R_S)$ is the drop surface tension attributed to the surface of tension we arrive finally at the following equation:

$$\ln S_1 = \frac{2V_{Bi}\sigma(R_S)}{kT R_S}. \tag{12}$$

One should note that if $\sigma(R_S)$ is a weak function of radius it is approximately equal to the surface tension σ_∞ of the flat interface and $R_S \cong R_e$ (where R_e is the equimolar radius). Then, in the case of nonassociated vapor Eq. (12) transforms to the classical Kelvin equation

$$\ln S = \frac{2V_{Bi}\sigma_\infty}{kT R_e}. \tag{13}$$

Equations like Eqs. (7)–(9) can be written for the chemical potentials of dimers as well. Then, we arrive at the following equation:

$$\ln S_2 = \frac{2V_{Bi2}\sigma(R_S)}{kT R_S}, \tag{14}$$

where V_{Bi2} is the volume per dimer in the phase β, $S_2 = \frac{P_2^\alpha}{P_2^{0,\alpha}}$ is the supersaturation of dimers, and P_2^α and $P_2^{0,\alpha}$ are the partial pressures of dimers in the phase α (and in the gas phase of real system far from interface) for the curved and flat interfaces, respectively.

Equation (14) can be obtained directly from Eq. (12). Indeed, Eq. (4) gives the following relationship:

$$S_1 = \sqrt{S_2}. \tag{15}$$

Then, substituting Eq. (15) in Eq. (12) and accounting that $V_{Bi2} = 2V_{Bi}$ we obtain Eq. (14). One should note that formulas derived in this section are valid for any associating vapor.

B. Evaluation of the nucleation volume, nucleation rate, and supersaturation ratio from the experimental measurements

As shown in Fig. 12 the vapor to wall deposition occurs at axial coordinate $z > -3.2$ cm which is in agreement with Fig. 13 demonstrating an increase of the light absorption at $z \approx -3.2$ cm. One should expect that the wall vapor deposition occurs at supersaturation $S > 1$. Therefore, it would be useful to evaluate the axial dependence of supersaturation ratio $S(z)$ just near the wall to find the area of $S \approx 1$. Thus, in the vicinity of the $S \approx 1$ zone the supersaturation can be roughly estimated as

$$S(z) \approx \frac{P_{av}}{P^0(T_{wall})} \approx \frac{F_0 k_B T_{room}}{Q_0 P^0(T_{wall})}, \tag{16}$$

where P_{av} is the average over the tube cross section vapor pressure, $P^0(T_{wall})$ is the saturated vapor pressure near the wall (see Table I), $F_0(s^{-1})$ is the rate of evaporation of molecules (both Bi and Bi_2) from the crucible in the isothermal zone, k_B is the Boltzmann constant, T_{room} is the room temperature, and $Q_0(cm^3\ s^{-1})$ is the gas flow rate at room temperature. The quantity F_0 was determined from the rate of evaporation of bismuth from the crucible and the $\frac{P^0_{Bi_2}}{P^0_{Bi}}$ ratio (Eq. (3)) in the isothermal zone. Then, using the experimentally measured wall temperature (see Fig. 2) we get the supersaturation ratio as shown in the inset of Fig. 13. One can see from the comparison of the $S(z)$ function with the light absorption curves and the wall deposit mass profile (Fig. 14) that indeed the wall deposition starts at about the supersaturation $S \approx 1$.

The following stages of the wall deposit formation can be selected. Initially, when the vapor + Ar flux is coming along the clean tube, in the region of $S > 1$ the nucleation starts first on the surface defects for which the work of formation of the critical nucleus is relatively low. This first stage of the wall deposition results in the formation of single islands (image 1 in Fig. 12). As the flux is coming further down, the supersaturation increases and the heterogeneous nucleation on smooth surface starts resulting in the dense deposit formation (image 3). The border between the islands and dense deposit is observed as a step-like increase of the absorption intensity in Fig. 13 (marked as arrows with number 1). Initially, this border propagates upflow with the deposition time (compare two lower curves in Fig. 13) and we observe islands with the dense deposit between them (image 2, Fig. 12) as a result. However, the supersaturation is less upflow and the border propagation is slowing down. On the other hand, the islands are growing up due to the vapor to island deposition and, finally, they merge together, forming a continuous layer of bismuth. As a result, the islands-to-dense deposit border fades out (Fig. 13, two upper curves). One should note that initially the rate of vapor deposition in the region of dense deposit is substantially higher than that in the region of islands. Therefore, the border between dense deposit and islands can be considered as a starting point for vapor to wall deposition in the numerical simulations for deposition time less than 1.5 h.

The second step-like increase of the absorption at $z \approx -0.5$ cm (marked as number 2 in Fig. 13) is deposition time independent. Therefore, it is reasonable to assume that the last increase is related to some process in the gas-phase. The light scattering data (Fig. 11) show that as the gas follows the tube the nucleation starts near the walls (and then the nucleation zone is spreading towards the axis). As the nucleation onset is just near the wall it is reasonable to expect for a step-like change of the wall deposit light absorption properties in the nearby location. Therefore, the coordinate $z \approx -0.5$ cm of wall deposit absorption increase can be attributed to the nucleation onset. The last conclusion is in an agreement with the "supersaturation cut-off" results. As seen from Fig. 16(a) in the range of $-3 < z < -0.5$ cm the aerosol outlet concentration is coming down (due to the vapor to grid deposition) with increasing z. However, at $z > -0.5$ cm the outlet concentration is increasing with z, which means that the particles are formed at about $z > -0.5$ cm. The reasonable agreement between Figs. 13 and 16(a) testifies that the "supersaturation cut-off" curves display correctly the nucleation zone. Therefore, one can assume that the nucleation zone is in the rage of $-0.5 < z < 5$ cm. As follows from Fig. 16(a) the range $-0.5 < z < 2$ cm can be attributed to the initial acceleration of nucleation near the walls (which is in agreement with Fig. 11 demonstrating the light scattering from particles near the walls at $z > 2$ cm). At the range $z \approx 3$ cm the "supersaturation cut-off" curve demonstrates a shoulder, which is probably related to the shift of the nucleation zone from the walls to the axis (which is in agreement with the numerical simulation results of Sec. IV C). Finally, as seen from Fig. 16(a) the nucleation is over at about $z \approx 5$ cm (in agreement with Fig. 11 which shows that near the axis the large particles are already formed at $z > 4.6$ cm).

Figure 18 shows the total flux F of bismuth over the tube cross section (both as vapor and particles) vs. the axial coordinate. The experimental points were determined as the difference between the experimental rate of bismuth evaporation (Fig. 9) from the crucible in the isothermal zone and the rate of wall deposition (as found from Fig. 14). As we are interested in the regions of supersaturated vapor in the chamber, where the Bi to Bi_2 equilibrium is heavily shifted to Bi_2, the flux F was calculated in units of Bi_2 molecules. The last point in the plot at $z = 32$ cm was determined from the rate of aerosol deposition to the Petrianov's filter. There are a few characteristic zones in this curve. At $z < -3$ cm (region AB) there is no change of bismuth concentration with z, i.e., there is no vapor to wall deposition because the vapor

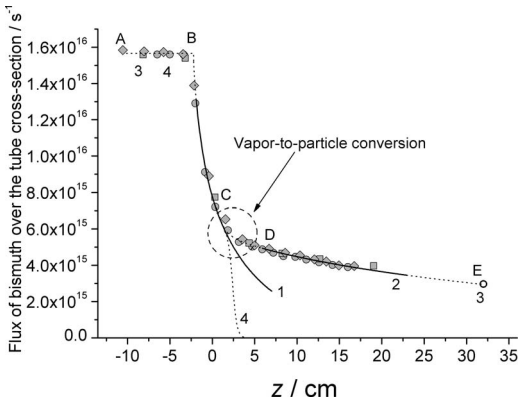

FIG. 18. The flux of bismuth through the tube cross section vs. the axial coordinate. $T_H = 1080$ K. Symbols: total flux $F(s^{-1})$ of Bi_2 molecules (both as vapor and constituents of aerosol particles). Filled symbols: evaluations from the difference between the evaporation and wall deposition rates (different symbols are from different experiments); open symbol: from the aerosol to filter deposition measurement. Solid line 1 is the numerical solution of Eq. (26) for the case of ω_{nucl} and ω_{cond} set as equal to zero; solid line 2 is the numerical solution of Eq. (28) for $z > 5$ cm (for $I_{nucl} = 0$) using the experimentally measured value of F at $z = 5$ as the boundary condition. The dotted lines 3 and 4 are the result of numerical simulation including all the stages: vapor to wall and particle to wall deposition, nucleation, coagulation, vapor to particle deposition; line 3 is the total flux of Bi_2 molecules (both as vapor and constituents of aerosol particles), line 4 is the flux of vapor Bi_2 molecules.

is undersaturated. At $-2.1 < z < 0$ cm (region BC) one can see a quick decrease of the flux magnitude with the increase of axial coordinate z (in agreement with Figs. 13 and 16(a)). This decay of the flux vs. z curve is due to the vapor to wall deposition as the vapor is supersaturated in this zone. On the other hand, at $z > 5$ cm (section DE) the flux does not change substantially with z. The only explanation of this fact is the vapor concentration being about zero at $z > 5$ cm. The weak decay of the function $F(z)$ in the section DE is, probably, due to aggregates to wall deposition owing to the thermal convection transfer. The section CD is the vapor to particle transition zone or, in other words, the nucleation zone. The location of the CD zone is in a reasonable agreement with the dip of "supersaturation cut-off" curve in Fig. 16(a) which supports our thesis that the nucleation occurs somewhere in the range $0 < z < 5$ cm.

The characteristic length of nucleation zone can be evaluated by the order of magnitude to be about 1 cm (lower estimate). For a rough estimation of the nucleation volume we assume that the nucleation zone circular cross section area is about the tube cross section (upper estimate) which gives the nucleation volume of about $V_{exp} \approx 0.3$ cm^3 (the same magnitude of V_{exp} is used in the following estimations for both $T_H = 1080$ and 1014 K). The absolute value of nucleation rate (the number of critical nuclei formed in unit volume per unit time) can be evaluated from the outlet concentration of particles and the nucleation volume. We refer to the nucleation rate determined in this way as the experimental nucleation rate $I_{exp.}$ The nucleation rate can be evaluated from the evident equation

$$I_{exp} V_{exp} = C_{aggr} \gamma_{prim} Q_0, \quad (17)$$

where C_{aggr} is the outlet concentration of aggregates as measured by ADB (Fig. 4(a)) and γ_{prim} is the mean number of primary particles per aggregate. Thus, for $T_H = 1080$ K accounting $C_{aggr} \approx 3.1 \times 10^8$ cm^{-3}, $\gamma_{prim} \approx 11$ (see Sec. III), and $Q_0 = 8.3$ cm^3/s we get from Eq. (17) $I_{exp} = 9.4 \times 10^{10}$ cm^{-3} s^{-1}. The quantity I_{exp} should be considered as a characteristic nucleation rate evaluated by the order of magnitude. However, as it will be shown in Sec. IV C, this accuracy is good enough as the quantity I_{exp} will be used to evaluate the surface tension of critical nucleus and an uncertainty of one order of magnitude in I_{exp} gives only 2% error in the magnitude of surface tension. As seen from Figs. 16(a) and 18 the axial coordinate $z = 2.5$ cm can be considered as the middle of the nucleation zone. As the nucleation starts at the wall and then shifts to the axis (see Fig. 11) the characteristic nucleation temperature is chosen as the average of axial and wall temperatures to be about $T_{exp} \approx 535$ K at $z = 2.5$ cm. It is evident that at the beginning of the nucleation zone (at $z \approx 0$ cm) the bismuth flux F can be considered as totally composed by the vapor and at the end of the nucleation zone ($z \approx 5$ cm) the vapor concentration is about zero. Therefore, for rough estimations one can put the mean vapor concentration in the middle of nucleation zone as half of that at the beginning. Following this assumption we estimate the supersaturation of dimers in the middle of nucleation zone as

$$S_{2,exp} \approx \frac{1}{2}\frac{P_{av}(0)}{P^0_{Bi2}(T_{exp})} = \frac{1}{2P^0_{Bi2}(T_{exp})}\frac{F(0)k_B T_{av}(0)}{Q_0 T_{av}(0)/T_{room}} = \frac{1}{2}\frac{F(0)k_B T_{room}}{Q_0 P^0_{Bi2}(T_{exp})} \approx 2.7 \cdot 10^8, \quad (18)$$

where $P_{av}(0)$, $T_{av}(0)$, and $Q_0 T_{av}(0)/T_{room}$ are the average over the tube cross section vapor pressure, temperature, and flow rate at $z \approx 0$ cm, respectively; $F(0)$ is the flux at $z \approx 0$ cm. Table II summaries the evaluated I_{exp}, $S_{2,exp}$, and T_{exp} for the heating temperatures $T_H = 1080$ and 1014 K for which the deposit mass profiles were available.

TABLE II. Nucleation rate, supersaturation, nucleation temperature, radius of the surface of tension, and surface tension of the critical nucleus as estimated from the "supersaturation cut-off" experiments.

T_H/K	T_{exp}/K	$S_{2,exp}$	I_{exp}/cm^{-3} s^{-1}	$R_{S,exp}$/ nm	σ_{exp} (mN/m)	$\sigma_{exp}/\sigma_\infty$
1080	535	2.7×10^8	9.4×10^{10}	0.459	478	1.25
1014	440	3.3×10^{11}	3.3×10^{10}	0.409	483	1.24

C. Numerical simulation

In Sec. IV B some approximate evaluations of the characteristic nucleation rate, temperature, and supersaturation were done basing on the experimentally measured temperature profiles, outlet aerosol concentration, and "supersaturation cut-off" data. These parameters will be later used to estimate the surface tension of critical nucleus. In the present section we will carry out a numerical simulation in order to retrieve the supersaturation and nucleation rate as functions of axial and radial coordinates and determine the surface tension of critical nucleus more exactly. We will discuss the calculation procedure and show that the calculation results are in a good agreement with the experimentally measured flux of bismuth over

the tube cross section as a function of z, outlet aerosol concentration, size of aggregates, and primary particles as well as the number of primary particles in aggregate. We will show that the calculated nucleation rate as a function of radial and axial coordinates is in a reasonable agreement with the "supersaturation cut-off" experiments and the measurements of light scattering from aerosol particles.

The numerical simulation software is written with Borland C++ Builder. An iterative finite difference method is used to solve coupled differential equations in the *Euler coordinates*. The calculations are made for the case of cylindrical symmetry using the experimentally measured temperature field $T(z,r)$ (r is the radial coordinate). A uniform grid is created which covers the ranges for axial and radial coordinates from z_{in} to z_{out} and 0 to R_0 (R_0 is the radius of chamber), respectively. The grid includs 40 points for the radial coordinate and 280 to 560 points (in dependence of the magnitude of the outlet coordinate z_{out}) for the axial one. The step for the radial coordinate is $r_0 = 8.5 \times 10^{-3}$ cm and for the axial one it is $z_0 = 0.1$ cm. One can see that the axial step gives the spatial error of 0.05 cm, which equals to that in the experimental measurements of the axial temperature profiles. The inner diameter of tube set in simulations is 0.68 cm. Thus, the total volume under simulation is subdivided to elementary cells of volumes V_{ij} (i and j are the sequence numbers of axial and radial points which run from 0 to i_{f} and j_{f}, respectively). The elementary cell of numbers (i, j) is limited by the axial cross sections with coordinates $z_{\text{in}} + z_0(i - \frac{1}{2})$ and $z_{\text{in}} + z_0(i + \frac{1}{2})$ and cylindrical surfaces with radii $r_0(j - \frac{1}{2})$ and $r_0(j + \frac{1}{2})$ for $0 < j < j_{\text{f}}$, $r_0(j_{\text{f}} - \frac{1}{2})$ and R_0 for $j = j_{\text{f}}$, and it is confined by the surface with radius $r_0/2$ for $j = 0$. The experimental axial and wall temperature dependences on coordinate z are approximated by sigmoidal functions to be used in simulations. The radial temperature profiles are approximated by the axially symmetric parabolic functions.

The formula for the flow velocity $\boldsymbol{w}(r, z)$ accounting the axial and radial temperature dependence can be obtained from the stationary continuity equation

$$-div(n_g \boldsymbol{w}(r, z)) = \frac{\partial n_g}{\partial t} = 0, \tag{19}$$

where $\boldsymbol{w}(r, z)$ is the vector of the gas flow velocity, and n_g is the number concentration of gas. In the case of constant viscosity coefficient the stationary gas flow is governed by the Navier-Stokes equation. For the low velocity in approximation of the incompressible gas the solution of this equation gives the Poiseuille profile, and for the room temperature we have

$$w_{z,\text{room}}(r, z) = 2\overline{w}_{z,\text{room}}(1 - (r/R_0)^2), \tag{20}$$

where $w_{z,\text{room}}(r, z)$ is the axial component of flow velocity at room temperature, and $\overline{w}_{z,\text{room}}$ is the room temperature flow velocity averaged over r. Equation (20) corresponds to the situation when the flow lines are parallel to the axis, i.e., the components of velocity vector $w_x = w_y = 0$. In our case the temperature and, as a consequence, the viscosity coefficient are functions of r and z. However, our numerical simulations are implemented under the approximation of the flow lines being parallel to the axis. In this case, the solution of Eq. (19) can be written in the form

$$n_g(r, z)w_z(r, z) = C(r), \tag{21}$$

where $w_z(r, z)$ is the axial component of flow velocity and the integration constant $C(r)$ is a function of r. The pressure along the flow lines is considered to be constant, therefore, we have

$$n_g(r, z)T(r, z) = const = n_{g,\text{room}}T_{\text{room}}, \tag{22}$$

where $n_{g,\text{room}}$ is the gas number concentration at room temperature (at the inlet of chamber). Equation (21) then leads to the expression

$$w_z(r, z) = C(r)\frac{T(r, z)}{T_{\text{room}}n_{g,\text{room}}}. \tag{23}$$

When the temperature tends to the constant value of T_{room} Eq. (23) must transform to the Poiseuille formula (Eq. (20)) and, therefore, the integration constant must be equal to

$$C(r) = n_{g,\text{room}}2\overline{w}_{z,\text{room}}(1 - (r/R_0)^2). \tag{24}$$

Therefore, finally combining Eqs. (23) and (24) we arrive at the formula for the axial flow velocity to be used in our numerical simulations

$$w_z(r, z) = 2\overline{w}_{z,\text{room}}(1 - (r/R_0)^2)\frac{T(r, z)}{T_{\text{room}}}. \tag{25}$$

As the numerical simulation deals with the supersaturated vapor where the fraction of Bi molecules is negligible the vapor is considered as consisting of Bi_2 molecules only. Thus, the following species are considered in the kinetic scheme: Bi_2 vapor molecules, Bi_2 molecules which are constituents of aerosol particles, primary particles, and aggregates which consist of primary particles (the number of primary particles in an aggregate can be one or more than one). The vapor to particle conversion process includes: vapor wall deposition, which is activated for $i > i_{\text{dep}}$ in our simulations, homogeneous nucleation, vapor to particle deposition (condensation), coagulation, and aggregate wall deposition. The position of i_{dep} was chosen in accordance with the experimentally measured wall deposit profiles (for $T_{\text{H}} = 1080$ and 1014 K) or "supersaturation cut-off" measurements (for $T_{\text{H}} = 920$ and 854 K). Thus, for example, as seen from Figs. 12 and 14, the wall deposition rate becomes significant at $z \approx -2.1$ cm (for the run time of 1.1 h), therefore, i_{dep} corresponds to that coordinate at $T_{\text{H}} = 1080$ K.

The concentrations of vapor, primary particles, and aggregates are determined solving the incompressible fluid continuity equations. For the vapor molecules this equation is

$$-div(\boldsymbol{F}_{\text{V}}) - \omega_{\text{nucl}} - \omega_{\text{cond}} = \frac{\partial n_{\text{V}}}{\partial t}, \tag{26}$$

where $\boldsymbol{F}_{\text{V}}$ is the flow density of Bi_2 vapor molecules, and ω_{nucl} and ω_{cond} are vapor consumptions in nucleation and vapor to particle deposition, respectively.

The continuity equations for primary particles and aggregates are

$$-div(\boldsymbol{F}_{\text{prim}}) + I_{\text{nucl}} = \frac{\partial n_{\text{prim}}}{dt}, \tag{27}$$

$$-div(\boldsymbol{F}_{\text{aggr}}) + I_{\text{nucl}} - \omega_{\text{coag}} = \frac{\partial n_{\text{aggr}}}{\partial t}, \tag{28}$$

where $\boldsymbol{F}_{\text{prim}}$ and $\boldsymbol{F}_{\text{aggr}}$ are the flow density of primary particles and aggregates, respectively, I_{nucl} is the nucleation rate, ω_{coag} is the rate of decrease of the aggregate concentration due to coagulation, and n_{V}, n_{aggr}, and n_{prim} are the vapor, aggregate, and primary particle number concentrations, respectively (n_{prim} is calculated for every elementary cell as the number of primary particles both as singles and in aggregates divided by the volume of cell). It is appropriate to mention that $n_{\text{prim}}(i, j) = n_{\text{aggr}}(i, j)\gamma_{\text{prim}}(i, j)$, where $\gamma_{\text{prim}}(i, j)$ is the mean number of primaries per aggregate in the cell with numbers (i, j).

The boundary conditions are set as follows. The Bi_2 vapor concentration: $n_{\text{V}}(0, j) = \frac{F_0}{Q_0}\frac{T_{\text{room}}}{T(0,j)} = \frac{F_0}{Q_0}\frac{T_{\text{room}}}{T_{\text{H}}}$, $n_{\text{aggr}}(0, j) = n_{\text{prim}}(0, j) = 0$ for $0 \le j \le j_{\text{f}}$; $n_{\text{V}}(i, j_{\text{f}}) = n_{\text{aggr}}(i, j_{\text{f}}) = n_{\text{prim}}(i, j_{\text{f}}) = 0$ for $i \ge i_{\text{dep}}$. When solving Eqs. (26)–(28) the initial concentrations of vapor molecules, primary particles, and aggregates are set as $n_{\text{V}}(i, j) = n_{\text{aggr}}\ (i, j) = n_{\text{prim}}(i, j) = 0$ for $i > 0$ and $0 \le j \le j_{\text{f}}$. As time evolves the aerosol and vapor concentrations tend to the stationary solutions. The criterion χ for the solution being stationary is the condition for the vapor concentration in any elementary volume

$$-\frac{1}{n_{\text{V}}}\frac{\partial n_{\text{V}}}{\partial t} < \chi = 10^{-11}\,\text{s}^{-1}. \tag{29}$$

When checking the sensitivity of the solution to the choice of criterion χ it was found that the increase of χ from 10^{-11} to 10^{-4} resulted in a change of all the calculated parameters (vapor and aerosol concentrations, mean diameters of aggregates and primary particles, mean number of primary particles per aggregate, etc.) by less than 10^{-3}%. The other indication to the choice of χ being correct follows from the fact that even at $\chi = 10^{-4}$ the iteration process is three times longer than the mean gas residence time.

Applying the theorem of Gauss to Eq. (26) leads to the following continuity equation for the grid cell(i, j):

$$\left[F^{\text{in}}_{\text{V},z}(i,j) - F^{\text{out}}_{\text{V},z}(i,j)\right]S_z(j) + F^{\text{in}}_{\text{V},r}(i,j)S^{\text{in}}_r(j) - F^{\text{out}}_{\text{V},r}(i,j)S^{\text{out}}_r(j) - \omega_{\text{nucl}}(i,j)V_{i,j} - \omega_{\text{cond}}(i,j)V_{i,j} = \frac{\partial N_{\text{V}}(i,j)}{\partial t}, \tag{30}$$

where $F^{\text{in}}_{\text{V},z}(i, j)$ and $F^{\text{out}}_{\text{V},z}(i, j)$ are the inlet and outlet axial components of the vapor flux for the cell (i, j), $S_z(j)$ is the jth axial cross section area, $F^{\text{in}}_{\text{V},r}(i, j)$ and $F^{\text{out}}_{\text{V},r}(i, j)$ are the inlet and outlet radial components of the vapor flux, $S^{\text{in}}_r(j)$ and $S^{\text{out}}_r(j)$ are the inner and outer cylindrical surface areas, $N_{\text{V}}(i, j)$ is the number of Bi_2 vapor molecules in the cell (i, j), and $\omega_{\text{nucl}}(i, j)$ and $\omega_{\text{cond}}(i, j)$ are consumptions of vapor molecules in nucleation and vapor to particle deposition, respectively. It is assumed the quantities $n_{\text{V}}(i, j)$, $\omega_{\text{nucl}}(i, j)$, and $\omega_{\text{cond}}(i, j)$ are constant over the cell. Similar equations are used in simulations for the numbers of aggregates and primary particles per elementary cell. Thus, at each iteration for every elementary cell we calculated number of Bi_2 vapor molecules ($N_{\text{V}}(i, j)$), the total number of Bi_2 molecules ($N_{\text{Bi2}}(i, j)$), the number of Bi_2 molecules which constituted particles ($N^{\text{part}}_{\text{Bi2}}(i, j)$), the numbers of primary particles ($N_{\text{prim}}(i, j)$) and aggregates ($N_{\text{aggr}}(i, j)$), the mean number of primaries in aggregates ($\gamma_{\text{prim}}(i, j)$) as well as concentrations $n_{\text{V}}(i, j) = N_{\text{V}}(i, j)/V_{i,j}$, $n_{\text{Bi2}}(i, j) = N_{\text{Bi2}}(i, j)/V_{i,j}$, $n^{\text{part}}_{\text{Bi2}}(i, j) = N^{\text{part}}_{\text{Bi2}}(i, j)/V_{i,j}$, $n_{\text{aggr}}(i, j) = N_{\text{aggr}}(i, j)/V_{i,j}$. The supersaturation ratio for dimers was calculated as $S_2(i, j) = n_{\text{V}}(i, j)k_BT(i, j)/P^0_{\text{Bi2}}(T(i, j))$ ($P^0_{\text{Bi2}}(T(i, j))$ is given in Table I). The mean mass of aggregates $M_{\text{aggr}}(i, j)$ and primaries $M_{\text{prim}}(i, j)$ was calculated for each cell as

$$M_{\text{prim}}(i, j) = \frac{N^{\text{part}}_{\text{Bi2}}(i, j)m_{\text{Bi2}}}{N_{\text{prim}}(i, j)}, \tag{31}$$

$$M_{\text{aggr}}(i, j) = M_{\text{prim}}(i, j)\gamma_{\text{prim}}(i, j), \tag{32}$$

where m_{Bi2} is the mass of Bi_2 molecule.

As the gas molecules axial diffusion is negligible with respect to the gas flow velocity, the axial component of the vapor flow density can be written as

$$F_{V,z}(z, r) = n_{\text{V}}(z, r)w_z(z, r). \tag{33}$$

The radial convective transport of vapor molecules is negligible with respect to the molecular diffusion transport; therefore, the radial component of the vapor flow density is given by[58]

$$F_{V,r}(z, r) = -\frac{D_{\text{Bi2}}}{k_BT}\left[\frac{\partial P_{\text{Bi2}}}{\partial r} + k_T\frac{P_{\text{total}}}{T}\frac{\partial T}{\partial r}\right], \tag{34}$$

where D_{Bi2} is the Bi_2 vapor molecules diffusion coefficient, P_{total} is the total pressure in the chamber ($P_{\text{total}} \approx P_{\text{Ar}} = 1$ atm), and k_{T} is the thermal diffusion ratio. The diffusion coefficient D_{Bi2} we estimated as[59,60]

$$D_{\text{Bi2}}(z, r) \approx 3.3 \times 10^{-6}T(r, z)^{1.75}\,\text{cm}^2/\text{s}. \tag{35}$$

The thermal diffusion ratio k_{T} can be evaluated via the following expression:[58]

$$k_{\text{T}} = x_{\text{Bi2}}x_{\text{Ar}}\frac{m_{\text{Bi2}} - m_{\text{Ar}}}{x_{\text{Bi2}}m_{\text{Bi2}} + x_{\text{Ar}}m_{\text{Ar}}}(2 - \varsigma), \tag{36}$$

where x_{Bi2} and x_{Ar} are the molar fractions for Bi_2 vapor and Ar, respectively, and $\zeta = 1.75$ is the power in Eq. (35) for the temperature dependence of diffusion coefficient. As $x_{\text{Bi2}} < 10^{-4}$ and $x_{\text{Ar}} \approx 1$ we have $k_{\text{T}} \approx x_{\text{Bi2}}\frac{m_{\text{Bi2}} - m_{\text{Ar}}}{m_{\text{Ar}}}(2 - \varsigma) = x_{\text{Bi2}}\frac{378}{40}0.25 = 2.36x_{\text{Bi2}}$.

The stationary solution of Eq. (26) for the case of ω_{nucl} set as equal to zero and $\boldsymbol{F}_{\text{V}}$ being governed by Eqs. (33) and (34) gives the flux axial profile governed by only vapor to wall deposition (line 1, Fig. 18) which is in a good agreement with the experimentally measured points in section BC. This good agreement allows concluding that Eqs. (34)–(36) are valid for Bi_2 molecules deposition process. One should note that the contribution of the thermal diffusion to the total vapor wall deposition is about 20% in our conditions. However, the line 1 is mismatching with the experimental points in the section DE. It is clear that the decay of the $F(z)$ curve in this section is due to the wall deposition of aggregates formed in the region CD.

The quantity ω_{nucl} in Eqs. (26) and (30) is the number of Bi_2 vapor molecules consumed in homogeneous nucleation per unit time and unit volume. To know ω_{nucl} one needs an analytical formula for the nucleation rate. The nucleation theory

gives the rate of nucleation from the supersaturated vapor[20]

$$I_{\text{nucl}} = K n_{\text{V}} \beta Z \exp\left(-\frac{4\pi R_S^2 \sigma_S(R_S)}{3k_{\text{B}}T}\right), \quad (37)$$

where n_{V} is the vapor concentration, K is the translation-rotation free energy correction factor (arising due to the so-called replacement free energy[26,27]), β is the collision frequency of vapor molecules with the critical nucleus, and Z is the so-called Zeldovich factor.

The classical nucleation theory assumes that the drop surface tension is equal to that of the flat interface (σ_∞). This simplification results sometimes in an error in the nucleation rate of tens to hundreds orders of magnitude.[20] Besides, it is set $K = 1$ in CNT. However, the direct numerical calculation shows that $K \approx 10^9$–10^{13} (for the L-J systems).[26] To obtain a rigorous analytical formula for the nucleation rate one should derive the formula for Zeldovitch factor Z accounting the dependence of drop surface tension on radius and an analytical expression for the correction factor K. Recently, we obtained the analytical formula for the correction factor in the framework of Frenkel theory of liquids, Reiss theory accounting the fluctuations of the drop center of mass, and Kusaka theory of replacement free energy.[27] We derived an analytical formula for the Zeldovitch factor[19,20,28] in the framework of the Nishioka and Kusaka thermodynamic theory of non-critical drop as well.[61] Thus, the rigorous formula for the rate of nucleation from the supersaturated bismuth vapor is

$$I_{\text{nucl}} = K n_{\text{V}}^2 \sqrt{\frac{2m_{\text{Bi2}}\sigma_S(R_S)}{\pi}} \frac{\varphi(x)}{\rho} \exp\left(-\frac{4\pi R_S^2 \sigma(R_S)}{3k_{\text{B}}T}\right), \quad (38)$$

where ρ is the density of the liquid macroscopic reference phase β, $x = \delta/R_{\text{S}}$, δ is the Tolman length which is equal to $\delta = R_e\text{-}R_S$ (in the case of a single component system), and $\varphi(x)$ is some function of x.[20] It was found that the $\varphi(x)$ can be set as equal to unity with the accuracy of 10%.[20] The analytical formula for the correction factor was derived from Ref. 27,

$$K = \frac{\pi^{7/2}}{n_{\text{V}}\sigma_R^3} \times \left(\frac{32R_S^5 \rho k_{\text{B}}T}{15h^2}\right)^{3/2} \times \exp\left(\frac{3h\nu_{\max}}{2k_{\text{B}}T}\right)\left\{1 - \exp\left(-\frac{h\nu_{\max}}{k_{\text{B}}T}\right)\right\}^3, \quad (39)$$

where h is Planck's constant, $\sigma_R \approx \frac{0.2}{(4\pi/3)^{1/6}}(\frac{m_{\text{Bi}}}{\rho R_S})^{1/2}$ is the standard deviation in any of the three Cartesian coordinates for the fluctuations of the center of mass of the drop embedded in the macroscopic reference phase β,[24,27] m_{Bi} is the mass of the Bi atom, and $\nu_{\max}$ and u are the Debye frequency ($\nu_{\max}^3 \approx \frac{u^3}{m_{\text{Bi}}}\rho$) and the sound velocity in the macroscopic liquid reference phase β, respectively. Then, for high temperatures the final formula for the nucleation rate can be written in the form

$$I_{\text{nucl}} \approx 3.4 \times 10^3 \pi^{7/2} n_{\text{V}} \frac{(u\rho)^3 R_S^9}{m_{\text{Bi2}}^2 (k_{\text{B}}T)^{3/2}} \sqrt{\sigma_S(R_S)} \times \exp\left(-\frac{4\pi R_S^2 \sigma_S(R_S)}{3k_{\text{B}}T}\right). \quad (40)$$

One should remember that the quantity n_{V} in Eq. (40) is the concentration of Bi_2 molecules.

The quantity ω_{nucl} is given by

$$\omega_{\text{nucl}} = I_{\text{nucl}} \frac{4}{3}\pi R_S^3 \frac{1}{V_{\text{Bi2}}}, \quad (41)$$

where V_{Bi2} is the volume per Bi_2 molecule in the liquid phase, and R_S is related to the surface tension and supersaturation S_2 by Eq. (14).

The vapor consumption in the vapor to particle deposition process is evaluated in the framework of kinetic collision theory

$$\omega_{\text{cond}} = \sigma_{\text{aggr}} \sqrt{\frac{8k_{\text{B}}T\left(m_{\text{Bi2}} + M_{\text{aggr}}\right)}{\pi m_{\text{Bi2}} M_{\text{aggr}}}} n_{\text{V}} n_{\text{aggr}}, \quad (42)$$

where σ_{aggr} is the collision cross section of Bi_2 molecules with aggregates. For the fractal-like dimension $D_{\text{f}} < 2$ the screening of primaries in aggregate is small enough[47,48] and, therefore, σ_{aggr} can be represented in the form

$$\sigma_{\text{aggr}} \approx \sigma_{\text{prim}} \gamma_{\text{prim}}, \quad (43)$$

where σ_{prim} is the collision cross section of Bi_2 molecules with primary particles

$$\sigma_{\text{prim}} = \pi(r_{\text{Bi2}} + r_{\text{prim}})^2, \quad (44)$$

where r_{prim} is the mean radius of primary particles and r_{Bi2} is the radius of Bi_2 molecules estimated as $r_{\text{Bi2}} = (\frac{4}{3}\frac{\pi\rho}{m_{\text{Bi2}}})^{-1/3} = 0.254$ nm. The mean radius of primary particles is calculated for each cell(i, j) as

$$r_{\text{prim}}(i, j) = \sqrt[3]{\frac{3}{4\pi}\frac{M_{\text{prim}}(i, j)}{\rho}}. \quad (45)$$

The vapor to particle sticking probability is set equal to unity.

As the axial diffusion for particles is negligible with respect to the gas flow rate, the axial component of the flux $\boldsymbol{F}_{\text{aggr}}$ (see Eq. (28)) can be written as

$$F_{\text{aggr,z}}(z, r) = n_{\text{aggr}}(z, r) w_z(z, r). \quad (46)$$

The flux vs. z curve decay in the range DE of Fig. 18 is due to the aggregate to wall convective deposition. In our numerical simulation it is convenient to write down the particle to wall convective deposition in the form of the Fick's law,

$$F_{\text{aggr,r}} = -D_{eff}\frac{\partial n_{\text{aggr}}}{\partial r}, \quad (47)$$

where D_{eff} plays the role of effective diffusion coefficient in the convective transport of aggregates to wall. The magnitude of D_{eff} governs the derivative of the flux vs. z curve at $z > 5$ cm. To estimate the magnitude of D_{eff}, we solved Eq. (28) numerically for $z > 5$ cm (under conditions of $I_{\text{nucl}} = 0$ and $\omega_{\text{coag}} = 0$). Then, the stationary solution for $D_{\text{eff}} = 0.01$ cm^2/s gives the curve 2 in Fig. 18 matching the experimentally measured flux. This value of the effective diffusion coefficient is used in the full scale numerical simulations for different heating temperatures. One should note that the value of D_{eff} obtained is about two orders of magnitude less than the vapor diffusion coefficient.

In order to retrieve the influence of thermophoresis on the particle velocity field, it is important to estimate the particle

to wall transfer due to temperature radial gradient. The thermophoretic velocity w_t can be estimated for the free molecular regime as[62]

$$w_t \approx 0.55\nu\frac{\nabla T}{T}, \tag{48}$$

where ν is the kinematic viscosity of Ar equal to[59]

$$\nu = 6.4 \times 10^{-6} T^{1.75}\,\mathrm{cm}^2/\mathrm{s}. \tag{49}$$

For typical temperature 700 K and $\nabla T \approx 750$ K/cm we have the thermophoretic velocity $w_t \approx 0.34$ cm/s, which is two orders of magnitude less then the axial flow velocity. Therefore, the thermophoretic transfer was not accounted separately in the numerical simulations. In any case, even if it is considerable it would be integrated in the effective diffusion coefficient D_{eff}.

The rate of decrease of the aggregate concentration due to the coagulation is calculated as

$$\omega_{\mathrm{coag}} = k_{\mathrm{coag}} n_{\mathrm{aggr}}^2, \tag{50}$$

where k_{coag} is the coagulation rate constant. To describe the coagulation of polydesperse aerosol the equivalent single size coagulation rate constant must be used which can be written as[62]

$$k_{\mathrm{coag}}(T) \approx \frac{4k_B T}{3\eta(T)} \times \left[1 + \exp(\ln^2 \sigma_g) + \frac{A(T)\lambda(T)}{r_{\mathrm{aggr}}}\exp(0.5\ln^2\sigma_g) + \frac{A(T)\lambda(T)}{r_{\mathrm{aggr}}}\exp(2.5\ln^2\sigma_g)\right], \tag{51}$$

where r_{aggr} is the aggregate mean radius, σ_g is the geometric standard deviation in the lognormal particle size distribution, $\lambda(T)$ is the mean free pass of the gas molecules, $\eta(T)$ is the gas dynamic viscosity, and $A(T)$ is the Cunningham correction factor constant. The temperature dependence of the dynamic viscosity for Ar is given by the formula[59]

$$\eta[\mathrm{Poise}] = 3.13 \times 10^{-6} T^{0.75}. \tag{52}$$

The temperature dependence of the Cunningham correction factor constant was determined in Ref. 63 for aerosol particles of different materials

$$A(T) = 1.257(T/295)^l, \tag{53}$$

where l can be expressed via the empirical formula

$$l = 1.03 + 0.57(1 + 10^{[(r_{\mathrm{aggr}}(\mathrm{nm})/0.19) - 10.45]})^{-1}. \tag{54}$$

$\sigma_g = 1.6$ is used in the simulations (see Sec. III and Fig. 7). The aggregate mean radius in Eq. (51) is evaluated in the calculations as

$$r_{\mathrm{aggr}} \approx r_{\mathrm{prim}} \gamma_{\mathrm{prim}}^{1/D_{\mathrm{f}}}. \tag{55}$$

The magnitude of fractal-like dimension $D_{\mathrm{f}} = 1.9$ is used as measured in TEM elaborations (see Fig. 6). The main physical-chemical parameters for bismuth used in the numerical simulations are given in Table I.

The nucleation rate as well as the surface tension are functions of $T(z, r)$ and $S(z, r)$ and, therefore, both of them can be written as functions of coordinates z and r. The function $I_{\mathrm{nucl}}(z, r)$ is exponential and, therefore, it must have a sharp enough maximum in the nucleation volume. Therefore, in the numerical simulations the function $\sigma_S(z,r)$ can be substituted by a constant close to the magnitude of $\sigma_S(z,r)$ in the point of maximum nucleation rate. The objective of numerical simulation is to fit this constant in such a way to bring in correspondence the calculated function $F(z)$ with the experimentally measured values. The flux of bismuth over the tube cross section is calculated as

$$F(z) = \int_0^{R_0} n_{\mathrm{Bi2}}(z, r) w_z(z, r) 2\pi r dr. \tag{56}$$

Figure 18 shows the calculated function $F(z)$ for $T_{\mathrm{H}} = 1080$ K in comparison with the experimental points. The flux of vapor Bi_2 molecules is also shown to compare. The other calculated parameters (outlet aggregate concentration, aggregate and primary particles mean diameters, and number of primaries per aggregate at the outlet of chamber) are compared with the experimental values in Table III. The outlet aggregate concentration is computed from

$$n_{\mathrm{aggr}}(z_{\mathrm{f}}) = \frac{1}{Q_0}\int_0^{R_0} n_{\mathrm{aggr}}(z_{\mathrm{f}}, r) w_z(z_{\mathrm{f}}, r) 2\pi r dr. \tag{57}$$

The outlet concentration of primaries $n_{\mathrm{prim}}(z_{\mathrm{f}})$ is determined similarly. The mean outlet diameters of aggregates and primaries are given as

$$d_{\mathrm{prim}}(z_{\mathrm{f}}) = 2\left(\frac{\int_0^{R_0} r_{\mathrm{prim}}^3(z_{\mathrm{f}}, r) n_{\mathrm{prim}}(z_{\mathrm{f}}, r) w_z(z_{\mathrm{f}}, r) 2\pi r dr}{\int_0^{R_0} n_{\mathrm{prim}}(z_{\mathrm{f}}, r) w_z(z_{\mathrm{f}}, r) 2\pi r dr}\right)^{1/3}, \tag{58}$$

$$d_{\mathrm{aggr}}(z_{\mathrm{f}}) = 2\left(\frac{\int_0^{R_0} r_{\mathrm{aggr}}^{D_{\mathrm{f}}}(z_{\mathrm{f}}, r) n_{\mathrm{aggr}}(z_{\mathrm{f}}, r) w_z(z_{\mathrm{f}}, r) 2\pi r dr}{\int_0^{R_0} n_{\mathrm{aggr}}(z_{\mathrm{f}}, r) w_z(z_{\mathrm{f}}, r) 2\pi r dr}\right)^{1/D_{\mathrm{f}}}. \tag{59}$$

The mean number of primaries per aggregate is found as $\gamma_{\mathrm{prim}}(z_{\mathrm{f}}) = n_{\mathrm{prim}}(z_{\mathrm{f}})/n_{\mathrm{aggr}}(z_{\mathrm{f}})$.

One can see from Table III that not only the calculated curve $F(z)$ is consistent with the experimental values but other calculated parameters are in a reasonable agreement with the experimental ones. This reasonable agreement allows assuming that the main stages of nanoparticle formation are formulated correctly in the simulation.

Figure 19 shows the supersaturation of dimers Bi_2 as a function of the axial and radial coordinates. It is to be mentioned that the maximum of the radial function of supersaturation is just near the wall. It is of interest to compare the function $S_2(z, r)$ with the dependency of nucleation rate on the radial and axial coordinates (Fig. 20). One should note that as the flux is moving along the tube, the nucleation starts near the walls, and then the maximums of the diametric profile shift from the walls to the axis with z increasing. Finally, at $z \geq 2.3$ the diametric profile demonstrates a single maximum

TABLE III. Comparison of the numerical simulation results with the experimental data.

T_H/K	Outlet axial coordinate/cm	Outlet aerosol concentration/cm^{-3}		Outlet diameter of aggregates/nm		Outlet diameter of primary particles/nm		Mean number of primary particles per aggregate (γ_{prim})	
		Expt.	Calc.	Expt.	Calc.	Expt.	Calc.	Expt.	Calc.
1080	32	$(3.1 \pm 0.5) \times 10^8$	2.5×10^8	80 ± 5	90.0	29 ± 2	28.8	11 ± 2	8.7
1014	18	$(2.9 \pm 0.5) \times 10^8$	2.9×10^8	45 ± 5	32.7	13 ± 1	14.7	4 ± 1	4.6
920	18	$(2.3 \pm 0.5) \times 10^8$	3.0×10^8	18 ± 3	13.9				
854	46	$(2.6 \pm 0.5) \times 10^7$	2.5×10^7	10 ± 2	7.3				

in the center. Let us denote the maximum of the radial profile of the nucleation rate as I_m and supersaturation, temperature, and radial coordinate corresponding to this maximum as $S_{2,m}$, T_m, and R_m, respectively. Figure 21 shows I_m, $S_{2,m}$, T_m, and R_m as functions of the axial coordinate. As can be seen at $z < 1.5$ cm the maximum I_m of the radial function $I_{nucl}(r)$ occurs just near the wall (Fig. 21(d)) where the supersaturation S_2 has reached a high value. The supersaturation $S_{2,m}$ increases and the temperature T_m decreases monotonously with z increasing in this region (Figs. 21(b) and 21(c)). In the range $1.5 < z < 2.3$ cm the maximum of the radial function $I_{nucl}(r)$ is shifting to the axis with z increasing. At the same time the supersaturation $S_{2,m}$ is coming down with z increasing but this decrease is overcompensated by the increase of T_m (as the axial temperature is higher than the wall one). As a result, the derivative dI_m/dz is the highest in the range $1.5 < z < 2.3$ and the function $I_m(z)$ comes to the maximum at $z = 2.35$ cm. At $z > 2.35$ cm T_m and I_m are coming down with z increasing, as the coordinate R_m of the maximum of the nucleation rate has reached the axis of the tube, and T_m follows now the axial temperature. The fact that the maximum of the function $I_m(z)$ is at $z \approx 2.35$ cm is in a good agreement with the "supersaturation cut-off" experiments, as this maximum corresponds to the middle of the dip in Fig. 16(a). Thus, the numerical simulation supports our confidence that the "supersaturation cut-off" measurements give the correct delimitation of the nucleation zone. As seen from Fig. 16(a) the "supersaturation cut-off" curve demonstrates some shoulder at $z > 1.5$ cm. From the comparison of Figs. 16(a) and 21 one can assume that the reason for this shoulder is related with the shift of the maximum of the radial function $I_{nucl}(r)$ from the wall to the axis.

As seen from Table IV $\sigma_S = 463.8$ mN/m was determined in the numerical simulation for $T_H = 1080$ K. It is important to bring this surface tension in correspondence with the other nucleation parameters, namely, the average supersaturation of Bi_2, temperature, and the radius R_S of the critical drop. Let us denote the total number of critical nuclei generated in the nucleation chamber per unit time as J

$$J = \int_V I_{nucl}(\boldsymbol{r}) dV, \tag{60}$$

where $\boldsymbol{r}$ is the radius vector of the center of volume dV. Then, the probability of nucleation in the elementary volume dV is

$$d\Omega(\boldsymbol{r}) = \frac{I_{nucl}(\boldsymbol{r})}{J} dV. \tag{61}$$

The average temperature, supersaturation of Bi_2, and the radius of the surface of tension can be found as

$$\langle T \rangle = \int T(\boldsymbol{r}) d\Omega(\boldsymbol{r}) = \frac{1}{J} \int_V T(z, r) I_{nucl}(z, r) 2\pi r dr dz, \tag{62}$$

$$\langle \log_{10} S_2 \rangle = \int \log_{10} S_2(\boldsymbol{r}) d\Omega(\boldsymbol{r}) = \frac{1}{J} \int_V \log_{10} S_2(z, r) I_{nucl}(z, r) 2\pi r dr dz, \tag{63}$$

$$\langle R_S \rangle = \int R_S(\boldsymbol{r}) d\Omega(\boldsymbol{r}) = \frac{1}{J} \int_V R_S(z, r) I_{nucl}(z, r) 2\pi r dr dz, \tag{64}$$

where $R_S(z, r)$ is calculated via Eq. (14). The average nucleation rate can also be computed as

$$\langle I_{nucl} \rangle = \int I_{nucl}(\boldsymbol{r}) d\Omega(\boldsymbol{r}) = \frac{1}{J} \int_V I_{nucl}(z, r) I_{nucl}(z, r) 2\pi r dr dz. \tag{65}$$

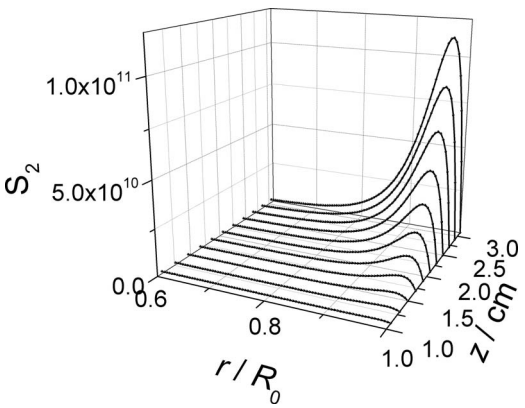

FIG. 19. Simulation results. Supersaturation of Bi_2 dimers as a function of axial and radial coordinates.

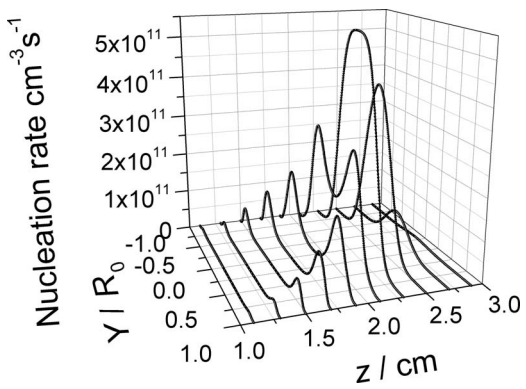

FIG. 20. Simulation results. Homogeneous nucleation rate as a function of axial (z) and diametric (Y) coordinates.

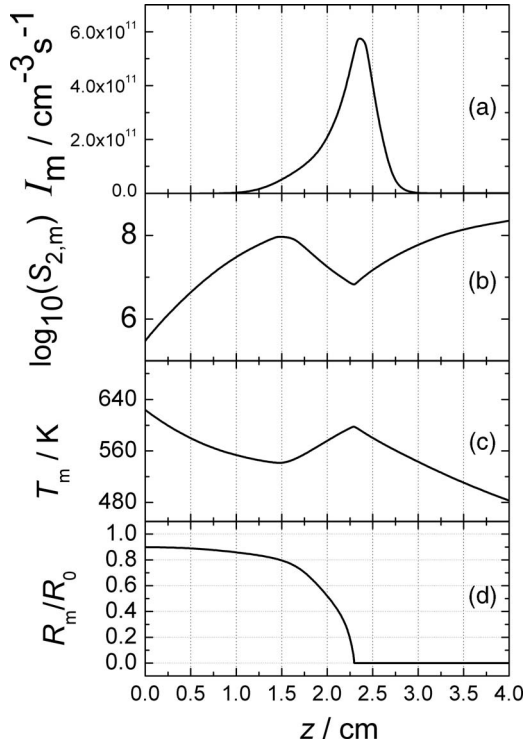

FIG. 21. Maximum I_m of the radial profile of the nucleation rate (a) and the corresponding maximum supersaturation $S_{2,m}$ (b), temperature T_m, (c) and radial coordinate R_m, vs. (d) axial coordinate.

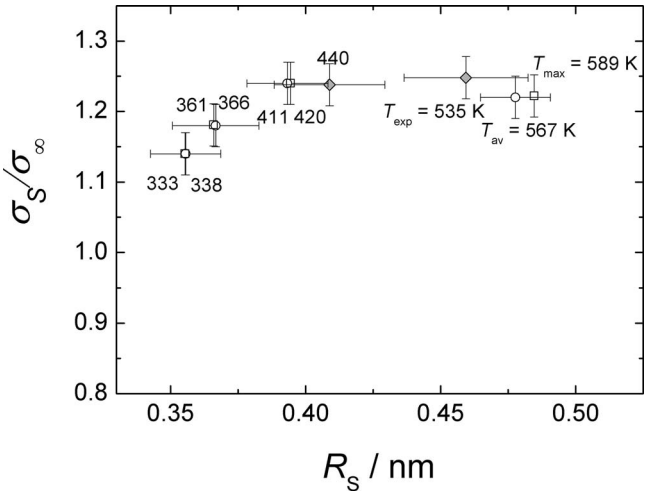

FIG. 22. The ratio σ_S/σ_∞ for different nucleation temperatures and values of the radius of surface of tension. Open symbols: numerical simulation results; filled symbols: direct estimation from the experimental data at $T_H = 1014$ and 1080 K. The average nucleation temperature is shown for the open circles, the temperature in maximum of the nucleation rate (T_{max}) for the open squares, and T_{exp} for the filled symbols.

The integration in the above formulas is made over the whole volume of the nucleation chamber. The average nucleation rate can be linked with the total rate J of production of critical nuclei via the evident equation

$$J = \langle I_{nucl} \rangle V_{eq}, \tag{66}$$

where V_{eq} is some equivalent volume which plays the role of the nucleation volume. These and other averaged parameters are shown in Table IV in comparison with the parameters corresponding to the maximum I_{max} of the function $I_m(z)$.

For two heating temperatures ($T_H = 1014$ and 1080 K) the nucleation rate (I_{exp}) as well as characteristic temperature (T_{exp}) and supersaturation ($S_{2,exp}$) were evaluated directly from the experimental data. Using the formulas (14) and (40) it is easy to calculate the surface tension σ_{exp} and radius of the critical nucleus $R_{S,exp}$ from I_{exp}, T_{exp}, and $S_{2,exp}$ (see Table II). It is of interest to compare the aforementioned experimental parameters with the numerical nucleation results (Table IV). As seen from this comparison the experimental and calculated values of nucleation rate are in a reasonable agreement. On the contrary, the calculated and experimental values of the nucleation temperature and supersaturation of Bi_2 are mismatching substantially. The reason in this mismatch is in quite approximate choice of the characteristic nucleation temperature T_{exp}. However, the experimental and calculated values of the surface tension are in a good concordance. This good accord is due to the fact that when overestimating the experimental nucleation temperature we automatically underestimate the supersaturation ratio (and vice versa). Therefore, the product $T^3(\ln S_2)^2$ in the exponent of the formula for the nucleation rate (which can be written when substituting R_S from Eq. (14) in Eq. (40)) is not much sensible to these inaccuracies. It was argued in Sec. IV B that the magnitude I_{exp} is determined with the order of magnitude accuracy, but, as can be found from Eqs. (14) and (40), the uncertainty in I_{exp} of one order of magnitude gives an error in σ_{exp} of 2% which is quite enough for approximate evaluations. The fact that σ_{exp} and the surface tension from the numerical simulation are in an agreement allows to conclude that simple evaluations from the "supersaturation cut-off" measurements give a correct value of $\sigma_S(R_S)$.

The surface tension can be considered as a function of its independent variables T and R_S.[1,64] Figure 22 shows the values of σ_S (fitted in numerical simulations) vs. the average radius of critical nucleus $\langle R_S \rangle$ for different heating temperatures. The magnitudes of σ_{exp} as well as $\sigma_S(I_{max})$ (as calculated from I_{max}, $S_2(I_{max})$, and $T(I_{max})$ using the formulas (14) and (40)) are also shown. The plotted points for the

TABLE IV. Nucleation parameters as calculated in numerical simulation.

T_H/K	$\langle T \rangle$/K	δT/K	$\langle \log_{10} S_2 \rangle$	$\langle I_{nucl} \rangle$/ cm^{-3} s^{-1}	$\langle R_S \rangle$/ nm	δR_S/ nm	V_{eq}/cm^3	σ_S(mN/m)	σ_S/σ_∞	I_{max}/cm^{-3} s^{-1}	$T(I_{max})$/K	$\log_{10}(S_2(I_{max}))$	$R_S(I_{max})$/ nm	N_{crit}
1080	567.0	25.81	7.47	2.2×10^{11}	0.477	0.013	0.15	463.8	1.22	5.8×10^{11}	588.6	7.03	0.484	13.2
1014	411.1	25.46	13.18	3.2×10^{10}	0.393	0.015	0.46	486.8	1.24	7.9×10^{10}	419.6	12.76	0.394	7.4
920	361.2	26.21	15.50	3.2×10^{10}	0.367	0.016	0.92	468.0	1.18	8.2×10^{10}	366.0	15.16	0.366	6.0
854	332.6	20.83	16.83	4.6×10^{9}	0.356	0.013	1.36	454.7	1.14	1.3×10^{10}	337.9	16.43	0.355	5.5

surface tension correspond to different values of the nucleation temperature. However, taking into account that the surface tension for flat surface is a weak function of temperature (and the plotted ratio σ_S/σ_∞ can be expected to be even weaker) one can assume that the plot of Fig. 22 reflects correctly the dependence of σ_S on radius R_S. A good agreement between the fitted surface tension and $\sigma_S(I_{max})$ is due to the nucleation being located in the narrow space. It is seen from Fig. 22 that the surface tension of critical nucleus is about 20% higher than that of the flat surface and changes weakly with R_S.

It is of interest to evaluate the number of Bi atoms inside the critical nucleus. As σ_S is a weak function of R_S the radius of the surface of tension is approximately equal to the equimolar radius R_e.[64] Therefore, the number N_{crit} of Bi atoms within the surface of radius R_S in the reference macroscopic phase β is approximately equal to the number of atoms in the critical nucleus being in the gas phase. As seen from Table IV N_{crit} is in the range of 6–13 for the heating temperature T_H being varying from 854 to 1080 K.

Now, it is possible to evaluate the correctness of our approach of σ_S being constant in the numerical simulations. Table IV shows the mean square deviations $\delta T = \sqrt{\langle T^2\rangle - \langle T\rangle^2}$ and $\delta R_S = \sqrt{\langle R_S^2\rangle - \langle R_S\rangle^2}$ for the temperature and radius R_S in the nucleation zone. The quantity δT does not exceed 26 K for the range of T_H from 854 to 1080 K. Accounting the temperature dependence for σ_∞ (Table I) it is easy to estimate that this value of δT corresponds to the variation of σ_∞ of about 0.5%. Assuming the temperature dependence of σ_S to be close to that of σ_∞ we can state that the temperature variation in the nucleation zone does not result in significant variation of σ_S. On the other hand, δR_S is only 3% of $\langle R_S\rangle$. This variation of R_S seems to be negligibly small, as we see from Fig. 22 the dependence σ_S on radius being very weak. Thus, we conclude that the dependence of the surface tension on the radius of the critical drop does not result in any serious contribution to the variation of σ_S as well. Therefore, our approximation of σ_S being constant seems to be reasonable enough.

It was discussed[19,20] that the elements of different groups of the Periodic Table demonstrate quite a different dependence $\sigma_S(R_S)$. The monovalent metals show σ_S/σ_∞ being considerably larger than unity decreasing with the increase of R_S. The bivalent metals demonstrate σ_S/σ_∞ being substantially less than unity independent of R_S in the range of temperature and supersaturation typical for the homogeneous nucleation experiments. As follows from the present work, bismuth, which is the element of the V group, demonstrates the surface tension of critical drop depending weakly on radius being larger than that for the flat surface.

V. CONCLUSIONS

Bismuth vapor homogeneous nucleation is studied experimentally in a horizontal laminar flow nucleation chamber at heating temperature T_H = 750–1150 K using the methods of TEM, SEM, automatic diffusion battery, light scattering, and others. The "supersaturation cut-off" technique is applied for bismuth vapor nucleation to determine the confines of the nucleation zone. Using the above experimental techniques the nucleation rate is determined to be $I_{exp} = 3 \times 10^{10}$ and 9×10^{10} cm^{-3} s^{-1} for the nucleation temperature $T_{exp} = 440$ and 535 K, respectively. To calculate the surface tension of critical nucleus and the radius of the surface of tension an analytical formula for the nucleation rate is used derived from Refs. 19, 20, 27, and 28, which is based on the Gibbs formula for the work of formation of critical nucleus and the translation-rotation correction. The values obtained are σ_{exp} = 483 and 478 mN/m and $R_{S,exp} = 0.409$ and 0.459 nm for the above nucleation temperatures, respectively. The surface tension estimated in this way is about 20% higher than that for a flat surface.

To determine the surface tension of critical drop from the experimentally measured bismuth mass flow rate, temperature profiles, ADB, and TEM data a more accurate approach is applied solving an inverse problem by numerical simulation. The simulation procedure includes the nucleation, vapor to particles and vapor to wall deposition, and particle to wall deposition, coagulation. The calculation results are in a good agreement with the experimentally measured wall deposit profile, mean size and concentration of the outlet aggregates, size of primary particles, and number of primaries per aggregate and, therefore, one can hope that the simulations give correct predictions for the nucleation rate, supersaturation, surface tension of critical nucleus, and the radius of the surface of tension. The nucleation rate is determined from simulations to be in the range of 10^9–10^{11} cm^{-3} s^{-1} for the supersaturation ratio 10^{17}–10^7 and nucleation temperature 330–570 K, respectively. The surface tension σ_S of the bismuth critical nucleus is found from simulations to be in the range from 455 to 487 mN/m for the radius of the surface of tension from 0.36 to 0.48 nm. The function σ_S changes weakly with the radius of critical nucleus. The value of σ_S is from 14% to 24% higher than the surface tension of a flat surface.

A good agreement between the nucleation rate, surface tension, and radius of the critical nucleus estimated from the "supersaturation cut-off" data with these parameters calculated numerically is observed. The agreement for the nucleation temperature and supersaturation of Bi_2 is not so good. Thus, the "supersaturation cut-off" method is appropriate for finding approximate values of σ_S and R_S. To find the nucleation temperature and supersaturation one need more exact numerical calculations.

ACKNOWLEDGMENTS

Financial support for this work was provided by Russian Federation for Basic Research (RFBR) Project No. 11-08-01204-a, the cooperation agreement between CNR (Italian National Research Council) and RAS (Russian Academy of Science) years 2011-2013, and joint research project between SB RAS and NSC Taiwan 2011–2013.

[1] J. W. Gibbs, *Thermodynamics and Statistical Mechanics* (Nauka, Moscow, 1982).
[2] V. G. Baidakov and G. Sh. Boltachev, Phys. Rev. E **59**, 469 (1999).
[3] I. Hadjiagapiou, J. Phys.: Condens. Matter **6**, 5303 (1994).

[4]D. J. Lee, M. M. Telo da Gama, and K. E. Gubbins, J. Chem. Phys. **85**, 490 (1986).
[5]M. A. Hooper and S. Nordholm, J. Chem. Phys. **81**, 2432 (1984).
[6]R. Guermeur, F. Biquard, and C. Jacolin, J. Chem. Phys. **82**, 2040 (1985).
[7]T. V. Bykov and A. K. Schekin, Inorg. Mater. (Russ.) **35**, 759 (1999).
[8]T. V. Bykov and A. K. Schekin, Colloid J. USSR **61**, 164 (1999).
[9]A. H. Falls, L. E. Scriven, and H. T. Davis, J. Chem. Phys. **78**, 7300 (1983).
[10]A. H. Falls, L. E. Scriven, and H. T. Davis, J. Chem. Phys. **75**, 3986 (1981).
[11]M. Iwamatsu, J. Phys.: Condens. Matter **5**, 7537 (1993).
[12]K. Koga, X. C. Zeng, and A. K. Shchekin, J. Chem. Phys. **109**, 4063 (1998).
[13]L. S. Bartell, J. Phys. Chem. B **105**, 11615 (2001).
[14]R. Bahadur and L. M. Russell, Aerosol Sci. Technol. **42**, 369 (2008).
[15]S. M. Thompson, K. E. Gubbins, J. P. R. B. Walton, R. A. R. Chantry, and J. S. Rowlingson, J. Chem. Phys. **81**, 530 (1984).
[16]J. Vrabec, G. K. Kedia, G. Fuchs, and H. Hasse, Mol. Phys. **104**, 1509 (2006).
[17]M. Horsch, J. Vrabec, and H. Hasse, Phys. Rev. E **78**, 011603 (2008).
[18]P. R. ten Wolde and D. Frenkel, J. Chem. Phys. **109**, 9901 (1998).
[19]A. A. Onischuk, P. A. Purtov, A. M. Baklanov, V. V. Karasev, and S. V. Vosel, J. Chem. Phys. **124**, 014506 (2006).
[20]S. V. Vosel, A. A. Onischuk, P. A. Purtov, and T. G. Tolstikova, "Classical nucleation theory: Account of dependence of the surface tension on curvature and translation-rotation correction factor," in *Aerosols Handbook. Measurement, Dosimetry, and Health Effects*, edited by L. S. Ruzer and N. H. Harley (CRC Press, Taylor & Francis Group, 2012).
[21]Y. I. Frenkel, *Kinetic Theory of Liquids* (Academy of Sciences, Moscow-Leningrad, 1959).
[22]J. Lothe and G. M. Pound, J. Chem. Phys. **36**, 2080 (1962).
[23]J. Lothe and G. M. Pound, J. Chem. Phys. **45**, 630 (1966).
[24]H. Reiss, J. L. Katz, and E. R. Cohen, J. Chem. Phys. **48**, 5553 (1968).
[25]H. Reiss, W. K. Kegel, and J. L. Katz, J. Phys. Chem. **102**, 8548 (1998).
[26]I. Kusaka, Phys. Rev. E **73**, 031607 (2006).
[27]S. V. Vosel, A. A. Onischuk, and P. A. Purtov, J. Chem. Phys. **131**, 2045 (2009).
[28]S. V. Vosel, A. A. Onischuk, and P. A. Purtov, J. Chem. Phys. **133**, 047102 (2010).
[29]F. T. Ferguson and J. A. Nuth III, J. Chem. Phys. **113**, 4093 (2000).
[30]J. Hecht, J. Appl. Phys. **50**, 7186 (1979).
[31]G.-S. Cha, H. Uchtmann, J. A. Fisk, and J. L. Katz, J. Chem. Phys. **101**, 459 (1994).
[32]J. A. Fisk, M. M. Rudek, J. L. Katz, D. Beiersdorf, and H. Uchtmann, Atmos. Res. **46**, 211 (1998).
[33]M. M. Rudek, J. L. Katz, and H. Uchtmann, J. Chem. Phys. **119**, 11505 (1999).
[34]J. A. Nuth, K. A. Donnelly, B. Donn, and L. U. Lilleleht, J. Chem. Phys. **85**, 1116 (1986).
[35]F. T. Ferguson, J. A. Nuth III, and L. U. Lilleleht, J. Chem. Phys. **104**, 3205 (1996).
[36]J. Martens, H. Uchtmann, and F. Hensel, J. Chem. Phys. **91**, 2489 (1987).
[37]H. Uchtmann, K. Rademann, and F. Hensel, Ann. Phys. **48**(1–3), S207 (1991).
[38]R. Badahur and R. B. McClurg, J. Chem. Phys. **121**, 12499 (2004).
[39]F. Römer and T. Kraska, J. Chem. Phys. **127**, 234509 (2007).
[40]S. L. Girshick, P. Agarwal, and D. G. Truhlar, J. Chem. Phys. **131**, 134305 (2009).
[41]N. Lümmen and T. Kraska, J. Aerosol Sci. **36**, 1409 (2005).
[42]A. A. Kirsch, I. B. Stechkina, and N. A. Fuchs, J. Aerosol Sci. **5**, 119 (1975).
[43]D. Gonzalez, A. Nasibulin, A. Baklanov, S. Shandakov, D. Brown, P. Queipo, and E. Kauppinen, Aerosol Sci. Technol. **39**, 1064 (2005).
[44]A. Ankilov, A. Baklanov, R. Mavliev, and S. Eremenko, J. Aerosol Sci. **22**, S325 (1991).
[45]A. A. Onischuk, S. di Stasio, V. V. Karasev, A. M. Baklanov, G. A. Makhov, A. L. Vlasenko, A. R. Sadykova, A. V. Shipovalov, and V. N. Panfilov, J. Aerosol Sci. **34**, 383 (2003).
[46]E. N. Rybin, M. E. Pankratova, and M. E. Kogan, J. Phys. Chem. (USSR) **3**, 769 (1975).
[47]S. K. Friedlander, *Smoke, Dust, and Haze* (Oxford University Press, New York/Oxford, 2000).
[48]R. J. Samson, G. W. Mulholland, and J. W. Gentry, Langmuir **3**, 272 (1987).
[49]A. A. Onischuk, V. P. Strunin, V. V. Karasev, and V. N. Panfilov, J. Aerosol Sci. **32**, 87 (2001).
[50]N. Riefler, S. di Stasio, and T. Wriedt, J. Quant. Spectrosc. Radiat. Transf. **89**, 323 (2004).
[51]S. N. Rogak, R. C. Flagan, and H. V. Nguyen, Aerosol Sci. Technol. **18**, 25 (1993).
[52]*Handbook on Lead-Bismuth Eutectic Alloy and Lead Properties, Materials Compatibility, Thermal-Hydraulics and Technologies*. Nuclear Energy Agency, No. 6195, Organisation for Economic Co-Operation and Development, Paris (2007), ISBN 978-92-64-99002-9.
[53]V. G. Muradov, O. N. Muradova, and E. Yu. Yablochkov, J. Appl. Spectrosc. **20**(6), 810 (1974).
[54]J. H. Kim and A. Cosgarea, Jr., J. Chem. Phys. **44**, 806 (1965).
[55]Y. Shoji, T. Matsui, T. Nagasaki, M. Kurata, and T. Inoue, "Vapor pressure measurements of lanthanum-bismuth alloys by mass-spectrometric aethod," Int. J. Thermophys. **21**, 585 (2000).
[56]R. Hultgren, P. D. Desai, D. T. Hawkins, M. Gleiser, K. K. Kelley, and D. D. Wagman, *Selected Values of the Thermodynamic Properties of the Elements* (American Society for Metals, Metals Park, OH, 1973).
[57]J. L. Katz, H. Saltsburg, and H. Reiss, J. Colloid Interface Sci. **21**, 560 (1966).
[58]D. A. Frank-Kamenetskii, *Diffusion and Heat Transfer in Chemical Kinetics* (Nauka, Moscow, 1987).
[59]*Physical Magnitudes*, edited by I. S. Grigoriev and E. Z. Meylikhov (Energoatomizdat, Moscow, 1991).
[60]B. V. L'vov and V. G. Nikolaev, J. Appl. Spectrosc. **46**(1), 1 (1987).
[61]K. Nishioka and I. Kusaka, J. Chem. Phys. **96**, 5370 (1992).
[62]P. C. Reist, *Aerosol Science and Technology* (McGraw-Hill, USA, 1993).
[63]V. Ya. Rudyak, S. N. Dubtsov, and A. M. Baklanov, J. Aerosol Sci. **40**, 833 (2009).
[64]R. C. Tolman, J. Chem. Phys. **17**, 333 (1949).